Graphical Abstract

The effect of combined yawed and turbulence intensity on the wake development and performance of a tidal stream turbine.

Matthew Allmark, Allan Mason-Jones, Jean-Valery Facq, Benoît Gaurier, Gregory Germain, Tim O'Doherty

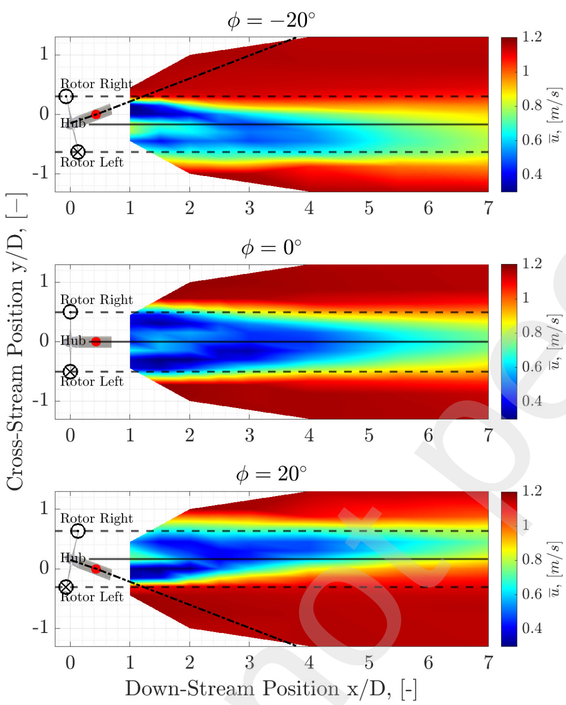

Highlights

The effect of combined yawed and turbulence intensity on the wake development and performance of a tidal stream turbine.

Matthew Allmark, Allan Mason-Jones, Jean-Valery Facq, Benoît Gaurier, Gregory Germain, Tim O'Doherty

- Detailed description of wake skew under yawed inflow.
- Detailed description of turbulent structures in the near-mid wake.
- Initial study into wake steering for HATTs.

The effect of combined yawed and turbulence intensity on the wake development and performance of a tidal stream turbine.

Matthew Allmark[a], Allan Mason-Jones[a], Jean-Valery Facq[b], Benoît Gaurier[b], Gregory Germain[b], Tim O'Doherty[a]

[a] *Cardiff School of Engineering, Cardiff University, Queen's Buildings, The Parade, Cardiff, CF24 3AA, Wales, United Kingdom*
[b] *Ifremer, Hydrodynamic Laboratory, 150 Quai Gambetta, Boulogne-sur-Mer, 62200, France*

Abstract

The development of wakes downstream of horizontal-axis tidal stream turbines is of interest because these devices, when installed in arrays, can generate predictable renewable energy. Specifically, wake development impacts both the performance of individual turbines and the overall turbine arrays, where upstream turbines can reduce the power output of downstream devices. Additionally, tidal flows are often not perfectly symmetric and can exhibit short-term variations in the predominant incoming flow angle.

This work presents the methods and findings of a lab-scale experimental campaign designed to characterize the wake structure under combined yaw and turbulent flow conditions. A 0.9 m lab-scale tidal turbine was subjected to low and high turbulent inflow characteristics, two yaw conditions ($\pm 20^{\circ}$), and a no-yaw case. The wake downstream of the device was recorded using a 3 component laser Doppler velocimeter, and these measurements were used to characterize the wake structure.

Under low turbulent conditions, yawing marginally improved wake recovery. In most yaw cases, wake skew was observed; however, the center-line progression of the wake was complex and influenced by the in-flow characteristics. Some degree of self-similarity in the flow was observed, which would presumably improve with downstream distance. Analysis of turbulence in the wake revealed a complex picture — with particularly high levels of turbulent kinetic energy at the blade tips under yawed flow conditions. The length scale of turbulence in the near to mid-wake was smaller than the rotor plane

length scales, and the return to isotropic conditions, which is assumed in many computational models, is complex and dependent on the anisotropy of the inflow turbulence.

Keywords: Tidal Energy, Horizontal Axis Tidal Turbine, Wake Measurement, Flume testing
PACS: 0000, 1111
2000 MSC: 0000, 1111

1. Introduction

The wakes of Horizontal Axis Tidal Turbines (HATTs) have been an active area of research for over a decade. Tidal flows are generally bi-directional with approximately 180° between ebb and flood flows, however some studies have shown misalignment of ebb and flood directions can be greater than ±20° but tend to fall within this range [1]. This can be due to local bathymetry, or the presence of headlands, tidal channels or larger features. Devices such as the SeaGen device pitched their turbine blades through 180°, but do not change the orientation of the turbine axis, and therefore the impact of flow misalignment on the turbine and the wake development downstream of devices needs to be assessed. Misalignment was identified early on by Bahaj et al. [2] as an issue which needed to be addressed by tidal turbine manufacturers. Furthermore, as tidal flows are predictable and periodic means there is ample scope for optimising the layout of tidal turbine arrays. This extends not only to a minimum distance between turbines in the main flow direction, but also allows more complex interactions to be considered, such as cross-stream spacing to take advantage of blockage effects, or alternating rotation directions to take advantages of swirl in the wake, or in the case of the research presented through utilising yaw misalignment to take advantage of wake meander.

A growing body of research has provided flow velocity measurements in the wakes of actuator discs [3], behind individual turbines [4], [5], [6] and in the wake of multiple devices [7] [8]. A central aspect of the experimental work produced so far have focused fully or in part on the effect of the turbulence levels in the on-coming flow on the device perfromance and wake development. The work of Maganga et al.[4] showed that an increase in turbulence intensity causes faster wake recovery, which was confirmed by [5], who concluded that, whilst an increase in ambient turbulence intensity only had a limited effect on the mean C_P and C_T, the wake was "deeply influenced" by the upstream turbulence, and that the "wake shape, length and strength largely depend on the upstream turbulence conditions". The work of Ebdon et al. [9] further developed this notion and considered the effect of operating tip-speed-ratio (λ) on the wake structure. This work also considered the effect of the method of characterising the wake width and length on the reported wake structure - i.e. showing that the wake width reported was highly dependent on the method of describing the wake boundary. Ebdon's work further corroborated the finding that ambient turbulence upstream of the device has a large effect on the wake recovery and further concluded that the manner in which one defines the wake width has a profound impact on the reported wake shape, with the later finding having a significant impact on the potential for the development of wake models for array optimisation [9]. A study with single turbines has also considered the effects of wide, shallow channels, to try and match possible geometric conditions in ocean channels, which found only small levels of asymmetry in the wake expansion [6]. A similar, high fidelity set of measurements using an Acoustic Doppler Velocimeter (ADV) in the wake of a turbine was published recently by Chen et al.[10], who measured to 20 diameters downstream of the rotor. This low ambient turbulence study with a relatively high blockage ratio of 16% by turbine swept area found that the centre-line velocity recovered to 90% of the free stream velocity approximately 11 diameters downstream of the rotor. As seen in a previous Large Eddy Simulation (LES) study [11], it was found that the stanchion had a significant influence over the wake in its immediate vicinity, but this was limited to the near wake region.

Another aspect of wake development which has received a good deal of attention are the development of turbulence characteristics within the wake. Turbulence characteristics such as turbulence intensity, decay rate and level of anisotropy are thought to play a central role in the wake recovery process as well as in the application of HATTs. Investigations into the turbulence produced in the near wake (between 1.5 and 7 diameters downstream of rotor) were made by Tedds et al. [12] who noted that the rotation of the turbine blades induced significant anisotropy into the turbulence, and suggested therefore that numerical models which rely on the assumption of isotropic turbulence (e.g. 2-equation RANS models) may struggle to accurately reproduce the flow in this region. It was also noted that the rate of decay of turbulence kinetic energy in the wake region was "significantly different to that observed downstream of grids, meshes or perforated disks, suggesting that previous modelling approaches, which neglected swirl effects and modelled the turbine by absorption discs, may significantly over predict the turbulent kinetic energy (k) decay rate of HATT wakes." [12]. This would suggest that the quantitative results of porous discs may not be directly applicable to tidal turbines, however, qualitative effects such as those noted by Blackmore et al. [13] could well still be applicable. Zhang et al. [14] also studied the homogeneity of the turbulence in the wake of a lab-scale tidal turbine.

A final aspect of wake development which has warranted attention are the characteristics of the near wake region, particularly with respect to measurements made in a phase locked manner to the turbine rotation. To this end, Morandi et al.[6] conducted a flume study where measurements were made immediately behind the turbine rotor. These measurements were phase-locked with the turbine's rotational frequency in order to identify how wake features relate to the position of blades. The study demonstrated the complexity of the near-wake structure, and also indicated that some features of the near-wake such as the strength of the tangential velocity component, are dependent on the turbine operating condition (tip-speed ratio). This was also found in the work presented by Ebdon et al [9].

One approach which has been pursued since the wide scale introduction of wind turbines (and subsequently as the field of tidal turbines has developed) is to attempt to find an analytical or empirical method for the prediction of the wake. The attraction of this approach is that a prediction of the effects of the wake without the need to resolve the flow-field around the turbine would potentially provide a quick method to predict the effects of a turbine on its surrounding environment. Early work in this area was conducted by Lissamann [15], who attempted to develop a "functional and dimensionally correct" analytical model of turbine wakes, based on known profiles of jets and plumes. Whilst no attempt was made to take into account the complex physical interactions in the wake (presumably due to the limitations of computational power at the time), Lissamann does include two turbulence terms – one for the ambient turbulence and one for the turbulence generated by the rotor itself, which are considered important to the development of the wake. These terms are tuned to the limiting cases of a plume and jet flow, and the model applied to wind farms to investigate farm power output for different configurations and wind directions, with agreement to real wind farms found to be reasonable considering uncertainties due to the instability of meteorological conditions and the limited physics contained within the model. Jensen [16] developed an analytical model based on mass conservation considerations to produce a 'top-hat' lateral profile of velocity deficit downstream of a wind turbine. The theoretical basis of this was adapted by Frandsen et al.[17] to include both momentum and mass conservation, and the resulting model applied to arrays of offshore wind turbines. The 'top-hat' profile, which underestimates velocity deficit at the centre of the wake, and overestimates it at the wake edges, was replaced by Bastankhah and Port´eAgel [18] with a Gaussian profile. This was shown to produce a better match to downstream velocity profiles behind a wind turbine, when compared to LES and experimental data.

Building on this work with wind turbine wakes, Lam and Chen [19] combined axial momentum theory across an actuator disc with flume measurements from Maganga et al. [4] to develop analytical equations for the prediction of the axial velocity deficit and its lateral distribution downstream of a tidal turbine. The equations for the wake prediction are based on work for ship propellers. These equations were then improved upon to take into account the effects of the turbine hub in order to predict the region of "double-dip" wake deficit seen in the near-wake region[70] in flows with low ambient turbulence intensity. The improved equations were compared to wake measurements made by Pinon et al. [20] in high ambient turbulence conditions, and showed good agreement for the far wake. This model, however, relies on using empirical data from the centreline velocity deficit of each turbine in order to calibrate it. The disadvantage of these empirical and analytical models lies in the fact that they are attempting to reproduce a wake using a relatively small number of input variables. Real wakes are dependent on many different factors and the complex physical interaction between these factors, and therefore, whilst these empirical and analytical models can produce wake predictions very quickly, their accuracy and ability to provide detailed information about the wake will necessarily be limited due to the simplicity of the underlying model. The accuracy can only be expected to suffer further as turbines are grouped together into arrays, and further complexities are added to the incoming flow such as vertical velocity shear profiles and ocean bathymetry.

This paper seeks to add to the body of knowledge by considering both wake structure and turbulence characteristics under combined inflow and yawed turbine conditions. This work seeks to add experimental data and findings to the research which will aid improved modelling and the development of low-cost wake optimisation approaches which maybe able to consider yaw. To date such a study has, to the best of the authors knowledge, not been completed.

The paper is organised as follows, in Section 2 the experimental design and apparatus is detailed, we then start the results by presenting the time averaged wake velocities (stream-wise and vertical) in Section 3.1. This is followed by presentation of an analysis of how the turbine wake, if considered as an axis-symmetric wake, adheres to self similarity laws in Section 3.2. Turbulence characteristics measured in the wake are then considered in Sections 3.3, 3.4 and 3.5, which inspect the turbulence kinetic energy generation and dissipation, the length scale of the turbulence generated and the isotropy and structure of the turbulence generated in the wake, respectively. Finally Section 4 summarises the main findings of the research.

2. Methodology

2.1. Experimental Setup

Figure 1 shows a photograph of the experimental apparatus used to study the impact of inflow turbulence and device yaw on the development of the flow structures in the wake of a lab-scale HATT. Figure 2 shows the setup as a series of plan-view schematics.

A lab-scale turbine was mounted on a 0.105 m diameter stanchion connected to a supporting structure above the $4 \times 2 \times 18$ m wave and current flume at IFREMER, Boulogne-sur-Mer, as shown in Figure 1. The turbine was mounted at three different yaw angles as designated in Figure 2a, the yaw angles tested were $0°, 20°$ and $-20°$. The hub height was set to 1 m below the water surface and centred in the cross-stream direction, at 2 m from each side wall, as seen in Figure 2.

The origin of the coordinate system used throughout the paper is shown in Figure 2 and sets the origin at the centre of the hub for the 0° yaw case. Yawing the device anti-clockwise was given a negative designation where the turbine hub moves in the negative y-direction. Finally, the z-direction is aligned with the vertical position in the water column, again with the origin at hub height for the 0° yaw case, downwards is designated as positive and upwards as negative.

For all cases the turbine stanchion was kept in a fixed position leading to movement of the rotor position laterally (y-direction), the position of the turbine hub and blade extremes will be presented in the charts where necessary, as illustrated in Figure 2. Finally, the points on the charts show where the flow velocity in the wake was measured via a 3-Dimension Laser Doppler Velocimeter (LDV).

Two broad inflow conditions were generated with similar stream-wise velocity magnitude but with significantly different levels of inflow turbulence intensity. This was achieved by repeating the tests twice with and without the flow straightener installed in the flume. The flow straighteners are used to straighten the flow direction, break down larger flow structures and reduce the overall turbulence level in the flow. The test cases with the flow straighteners are designated the Low Turbulence Intensity (LTI) cases and the tests without the flow straighteners are designated High Turbulence Intensity (HTI) cases.

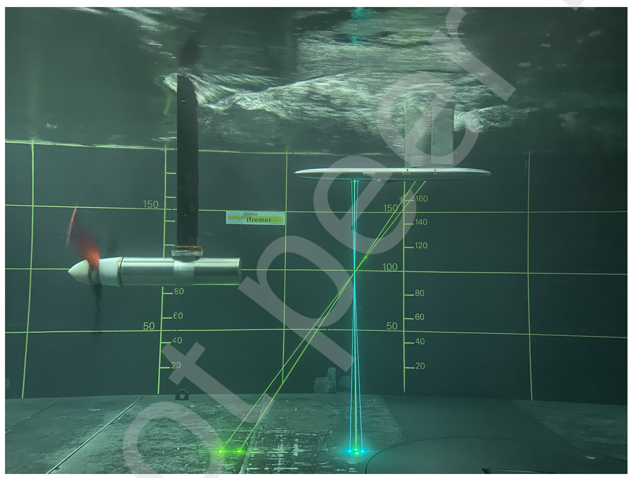

Figure 1: A photograph of the test setup at the IFREMER test facility, the photo shows the lab-scale tidal turbine and the 3-D LDV measurement apparatus used - the picture shows a measurement being taken in the near wake $x/D = 2$.

2.2. Lab-Scale Tidal Device

The lab-scale turbine utilised in the experiments presented herein was developed by Allmark et al [21] and has been tested thoroughly under a variety of flow conditions, including wave flows [22] [23] [24], profiled flows [25], wake flows [9] and turbulent flows [8]. The device used is one of three produced and is of 0.9 m diameter, utilising blades created with a modified Wortmann FX63-137 airfoil, the exact blade details can be found in [26]. The device is controlled by a Permanent Magnet Synchronous Machine (PMSM) which can be operated in speed or torque (load) control - for these experiments speed control was used to maintain a stable rotational velocity within ±1 RPM of the target. The Permanent Magnet Synchronous Machine (PMSM) was mounted in a direct-drive configuration where the rotational velocity was measured via an encoder which was utilised for vector oriented control [24]. A torque/thrust transducer developed by Applied Measurements is mounted within the drive-train directly behind the turbine rotor, upstream of any seals or bearings. Blade root bending moments are measured on each blade using a series of full-bridge strain gauges, installed by Applied Measurements - the signals for the bridge are amplified in the turbine nose cone. The data was collected by various data acquisition cards mounted within a National Instruments Compact Rio and sampled at 200 Hz.

2.3. Wake Measurement

A 3-Dimension Laser Doppler Velocimeter (LDV) system was used to measure the fluid velocity at the turbine rotor plane and throughout the near-to-mid wake. The 3D LDV system used 6 laser beams to measure three components of the fluid velocity, u, v and w, aligned with the x, y and z axes, respectively - see Figure 2. The lasers used to measure the flow had wavelengths of 514 nm, 466 nm and 532 nm with the raw data requiring projection onto the x, y and z axis. The 3D LDV requires that the flume tank is seeded with reflective particles which in this case are silver coated glass particles of 10 μm diameter - the particles are small enough to have minimal impact on the flow but large enough to reflect enough light to achieve a good signal-to-noise ratio. The 3D LDV has a variable sample rate, as a seeding particle must pass through two converging lasers to make a measurement. The sample rate is therefore related to the number of seeding particles used and for these experiments the level of seeding resulted in an average sample rate of 182 Hz. However, to process the data consistently the readings were re-sampled to a common sample rate of 170 Hz.

The flow velocity at the rotor plane (without the turbine installed) was measured prior to the experiments with 3D LDV mounted inline with the eventual rotor location, measuring various points in a cross formation spanning the device rotor. The locations of the measurement points are also shown in Figure 2b and 2b.

For each yaw angle and turbulence intensity combination the near to mid wake of the turbine was measured via a 3D LDV. The near-to-mid wake was measured, with the turbine set to a fixed rotational velocity, and the points measured are highlighted in Figures 2b and 2c. For each wake map the turbine was operated at approximately 75 RPM or 7.85 rad/s which resulted in an average tip-speed ratio (λ) of $\lambda = 4$ which has been previously found to give peak power output for the lab-scale turbine [21]. During the LTI cases the 3D LDV data was captured for 150 s whereas for the HTI cases each wake point was recorded for 300 s.

2.4. Rotor Plane Conditions

The recirculating flume was setup to have an upstream velocity of, $u_\infty \approx$ 1.1 ms^{-1} and the tests were undertaken with and without honeycomb flow straighteners installed to give two test cases, LTI (with straighteners, $TI \approx$ 2%) and HTI (without flow straighteners, $TI \approx 15\%$).

Here, $\overline{u}$ is the time averaged stream-wise velocity derived from the 3D LDV measurements by Equation 1, where Δt is the time period between subsequent samples and N is the number of sample points, finally $u(t)$ is the stream-wise fluid velocity recorded via the 3D LDV at a given location - similar expressions were used to average the v and w velocity components to give $\overline{v}$ and $\overline{w}$. The 3 dimensional Turbulence Intensity (TI) is given by Equation 2.

An estimation of the integral time scale, $\mathcal{T}$, was achieved by numerically integrating the auto-correlation function over time from 0 to T_0, where T_0 represents the time lag corresponding to the first zero-crossing of the auto-correlation function [27]. Subsequently, the integral length scale can be determined using the formula $\mathcal{L} = \overline{u_\infty} \cdot \mathcal{T}$. The auto-correlation and the integral used to develop an estimate of $\mathcal{T}$ are defined in Equations 3 and 4, respectively.

The resultant inflow conditions measured at the turbine rotor plane prior to installation are displayed for the LTI and HTI cases against cross-stream position and vertical position in Figures 3 and 4, respectively. Table 1 shows the resultant inflow characteristics averaged over the turbine rotor.

Figures 3 and 4 show that consistent results were achieved with the flume settings yielding two test cases with two varying levels of turbulent inflow as desired. However, in the process of removing the flow straighteners an overall rotation is imposed on the flow - this can be seen in the flow profile for $\overline{w}$ in Figure 3b and the flow profile observed for $\overline{v}$ in Figure 4b. The rotation of the flow is of an opposite orientation to the rotational velocity of the lab-scale turbine. Therefore the rotation imposed on the flow by the HATT rotor will be in the same sense or direction as overall rotation of the flow. As this rotation was unavoidable without excessive additional time and

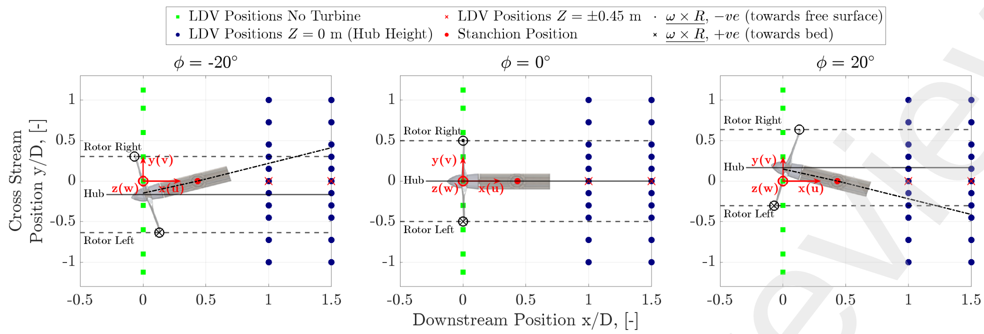

(a) Turbine orientations

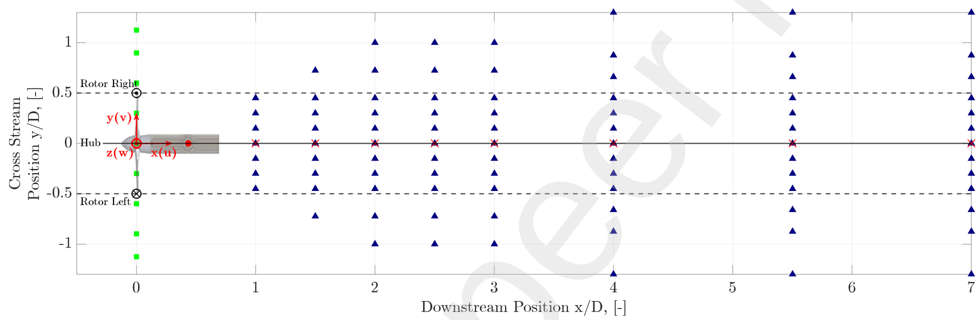

(b) LDV measurement positions, LTI Cases.

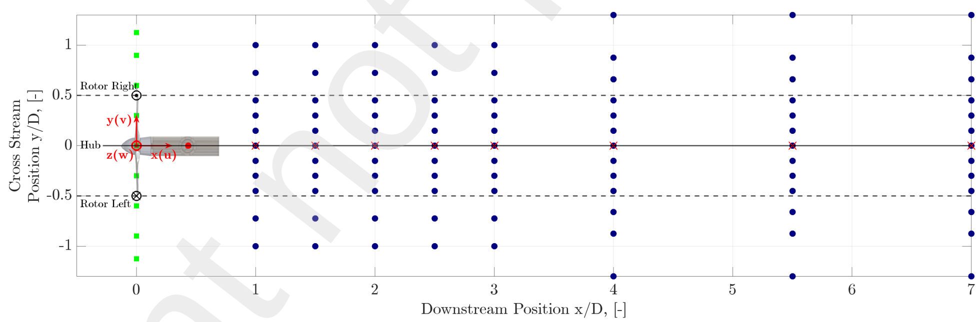

(c) LDV measurement positions, HTI Cases.

Figure 2: Schematic of the LDV measurement points for turbulence level and the turbine postions for each of the yawed flow cases, (a) shows the measurement positions for the LDV under the LTI cases, (b) shows the LDV measurement positions under the HTI cases and (c) shows the turbine positions for the three yaw angle setting. Note: the green squares show the rotor plane survey measurement positions, which were taken prior to the turbine installation for both the LTI and HTI cases, ⊙ illustrate a vector pointing out of page and ⊗ illustrates vector pointing into the page.

expense, the testing proceeded and the impact of the overall flow rotation is discussed throughout as required.

$$\overline{u} = \frac{1}{T}\int_{t=0}^{t=T} u(t) \approx \frac{\Delta t}{2}\sum_{i=0}^{i=N}(u(t)+u(t+\Delta t)) \quad (1)$$

$$TI = \frac{\sqrt{\frac{1}{3}(u'^2+v'^2+w'^2)}}{\sqrt{\overline{u_\infty}^2+\overline{v_\infty}^2+\overline{w_\infty}^2}} \times 100 \quad (2)$$

$$\mathcal{T} = \int_0^{T_0} R(t')\cdot dt' \quad (3)$$

where

$$R(t') = \frac{\overline{u'(t)u'(t-t')}}{\sigma_u^2} \quad (4)$$

Table 1: Average flow characteristics at the rotor plane before installation of the turbine.

	LTI	HTI
$\overline{u_\infty}$	1.08 m/s	1.05 m/s
TI	1.48 %	13.06 %
$\mathcal{L}$	0.83 m	0.58 m

2.5. Reynolds, Froude Number Scaling and Blockage Ratio

In developing lab-scale experiments care should be taken when scaling dynamic, kinematic and geometric aspects, to ensure the results can be utilised at full-scale. To this end both the Reynolds number (Re) and Froude number (Fr) were considered when developing the experiments.

Re quantifies the ratio of momentum forces to viscous forces within a given flow and is defined as used here in Equation 5. It is generally infeasible to achieve Re number equality between lab-scale and large scale testing, however many non-dimensional parameters have been shown to become Re independent for Re values between 0.5×10^5 to 1×10^5, depending on the rotor geometry [28]. The Re for the experiments developed, based on the chord length at $r/R = 0.7$ was $Re_{0.7} = 0.9 \times 10^5$, which has been shown previously to develop a flow regime whereby non-dimensional power and loading coefficients become independent of Re [28].

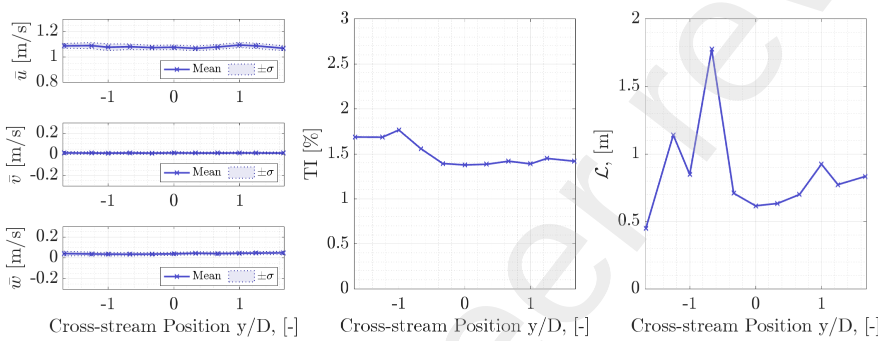

(a) Rotor plane flow characteristics with cross-stream position, LTI Cases

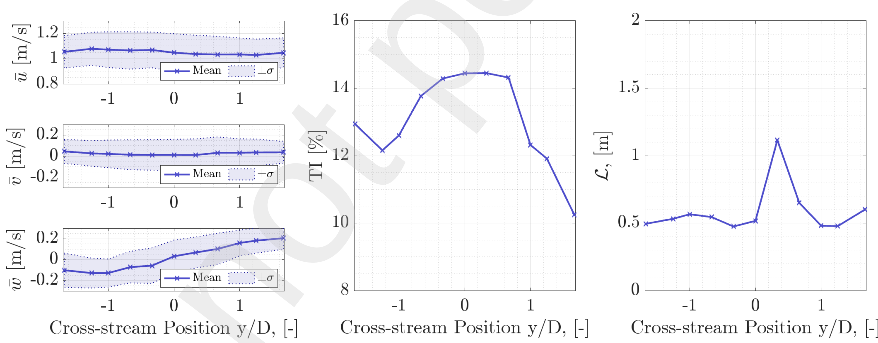

(b) Rotor plane flow characteristics with cross-stream position, HTI Cases

Figure 3: The inflow characteristics (U, TI and $\mathcal{L}$) recorded at the Rotor plane of the lab-scale tidal turbine plotted against cross-stream position.

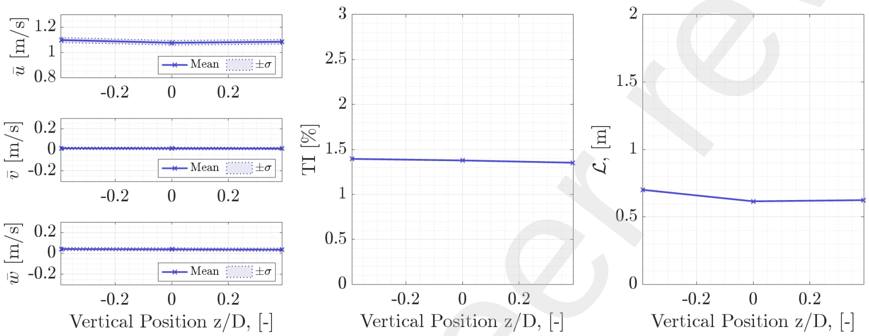

(a) Rotor plane flow characteristics with vertical position, LTI Cases

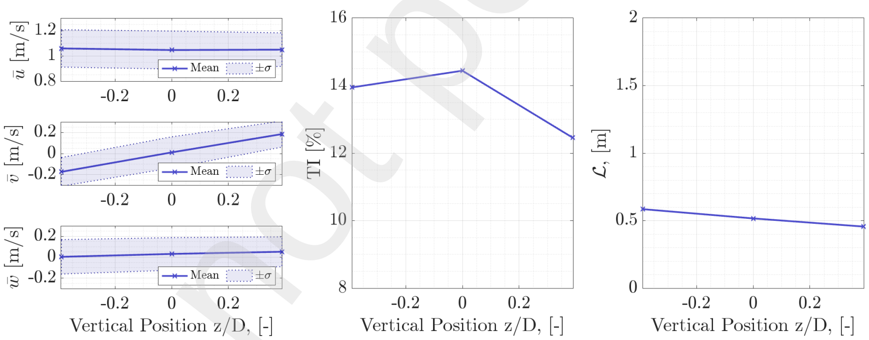

(b) Rotor plane flow characteristics with vertical position, HTI Cases

Figure 4: The inflow characteristics (U, TI and $\mathcal{L}$) recorded at the Rotor plane of the lab-scale tidal turbine, plotted against vertical position.

$$Re = \frac{\rho \overline{u_\infty} C_{0.7}}{\mu} \tag{5}$$

Fr quantifies the relative impact of inertial forces relative to gravitational forces and is calculated here using the hub depth and free-stream velocity using Equation 6. Fr for the testing setup described was $Fr_{Lab} = 0.25$. This is compared to Fr numbers ranging between 0.15 and 0.21 for large scale tidal devices operating in flows of 3 ms^{-1} at hub depths between 20 and 40 m. This is inline with the values reported in literature ($Fr = 0.143$ in [29]) and together with the Re number achieved, the test are thought to balance of the dynamics of inertial, viscous and gravitational forces appropriately.

$$Fr = \frac{v}{\sqrt{g \cdot D}} \tag{6}$$

The blockage ratio, B is utilised to acknowledge that in flume testing the flow is constrained by the flume walls when compared to the open ocean. Numerous studies have shown that more fluid is forced through the rotor, as it is unable to freely pass around the rotor due to the flume walls, and therefore elevated power and loading values are recorded [30][31][32]. Similarly, the effect of the flow being constrained also impacts the development of flow in the wake of a given HATT - however for wind turbines it has been shown that blockage ratios of < 0.09 have minimal impact wake mixing whereas blocakge ratios if 0.2 had a significant impact on mean stream-wise velocity in the wake [33]. The blockage ratio used here is given by Equation 7, where A_t is the swept area of the turbine rotor and A_F is the cross-sectional area of the flume. For the testing detailed herein a blockage ratio of $B = 0.08$ or 8% was achieved.

$$B = \frac{A_t}{A_F} \tag{7}$$

2.6. Thrust Coefficient and Blockage Correction

As the blockage level of, 8%, was fixed and unavoidable, blockage correction of the rotor non-dimensional thrust coefficient, C_T, was considered. Here, the C_T is defined in Equation 8, where u_∞ is the rotor plane velocity prior to turbine installation. The blockage correction developed by Bahaj et al was used [2] to correct the thrust coefficient to represent the turbine performance in an unbounded flow. The C_T values, both measured and corrected are given in Table 2. Here, the authors note that the levels will have an effect on the wake progression, where observable these effects are noted throughout.

$$C_T = \frac{T}{\frac{1}{2}\rho A_t u_\infty^2} \tag{8}$$

Table 2: Thrust Coefficient, C_T, before and after blockage correction for both LTI and HTI cases.

	Measured C_T	Blockage Corrected C_T
LTI, $\Phi = 0°$	0.988	0.900
LTI, $\Phi = 20°$	0.924	0.854
LTI, $\Phi = -20°$	0.926	0.860
HTI, $\Phi = 0°$	0.993	0.903
HTI, $\Phi = 20°$	0.917	0.849
HTI, $\Phi = -20°$	0.935	0.862

3. Wake Characteristics

3.1. Time-Average Flow Velocities

This section presents a summary of the wake structures measured in terms of the average velocity and velocity deficit in the principle orientations of interest, x (u) and z (w). The results of applying Equation 1 to the measured flow data are presented in Figures 5 to 8 for a horizontal plane, positioned vertically at the rotor hub centre. Figure 5 shows the velocity deficit derived from the average stream-wise fluid velocity measured, the deficit u^* is given by Equation 9. Figure 7 shows the specific time-averaged vertical flow velocity $\overline{w}$, for each wake transect undertaken. In both Figure 5 and 7 the results of the rotor plane map measurements, as detailed in Figure 2, are shown in black. Figures 6 and 8 show linearly interpolated wake maps with the turbine orientation and rotational axis highlighted.

$$u^*(x, y) = 1 - \frac{\overline{u(x, y)}}{\overline{u_\infty}} \tag{9}$$

Firstly, we consider the stream-wise velocity wake structure, which is of significance for array spacing, see [8] [34] [9]. An obvious finding shown in both Figure 5 and 6 is that the ambient turbulence has a profound effect on the wake recovery rate. During the LTI cases the wake deficit was found to be significant at $x/D = 7$, whereas this deficit was heavily diminished at the same point for the HTI cases, this can be clearly seen for each yaw angle case. This finding is inline with previous work undertaken in the area [9]. This finding is relatively intuitive as the increased ambient turbulence levels in the HTI cases led to greater mixing of the slowed wake flow and accelerated bypass flow at the wake extremes which leads quicker wake recovery. Yawing the turbine was not found to have a significant impact on the wake recovery rate in the stream-wise direction for either turbulence intensity case.

In the LTI cases the asymmetry in blockage introduced under the yawed cases led to a very slight asymmetry in the bypass flow where a marginally elevated value of the bypass flow was observed on the side with the smaller tip clearance to the flume side created in the yawing process. For example, in the $\phi = 20°$, LTI case, on the left hand side the deficit was $u^* = -0.06$, whereas on the more constrained right hand side the deficit was $u^* = -0.09$, where negative values show an increase in flow velocity. In the HTI cases, there was an overall asymmetry to the bypass flow regime, which persists regardless of the yaw angle and associated asymmetrical flow constraint - for example in the $\phi = 0°$ case, on the left of the turbine $u^* = 0.09$ was observed and on the right $u^* = 0.04$. The left hand bias in this case maybe related to asymmetry in the upstream flow introduced by the removal of flow straighteners which has already been observed in the Section 2.3. The accelerated bypass flow diminished more quickly in the HTI case compared to the LTI due to the increased mixing in the shear layer enabled by the turbulence in the flow.

In the near wake, $1 < x/D < 2$, the particular contributions of the hub and blade tips to the wake can be seen, particularly at $\phi = 0°$. These structures have been shown to be heavily dependent on the λ-value setting for the experiments. The structures from these individual effects were observed for larger x/D in the LTI cases ($x/D = 2.5$) and were less persistent in the HTI cases, where they were less prominent at the $x/D = 1.0$ and were destroyed by $x/D = 1.5$. In the yawed cases the effects of the turbine hub/nacelle and the blade tip structures, created when shadowing the hub/nacelle, were merged. This led to a combined larger deficit at the tank centre line (between hub and right blade extreme for $\phi = -20°$ and between hub and left blade extreme for $\phi = 20°$). These merged artefacts were dissipated over similar distances as the separate blade and hub deficits in the $\phi = 0°$ yaw case - this was true of both the LTI and HTI cases, where rotor/nacelle specific deficits were destroyed by $x/D = 2.5$ and $x/D = 1.5$, respectively.

The stream-wise velocity map shown in Figure 6 highlights the degree of wake skew observed in the experiments. Here, wake skew is defined as the angle between the turbine rotational axis and the wake axis. The wake maps show that for the LTI cases the orientation of the wake skew was generally found to be inline with momentum theory, i.e. the wake axis is deviated from the stream-wise flow axis in the opposite direction to the turbine yaw direction [35]. Here this deviation can be explained by the reaction force applied by the turbine rotor to the flow which will be equal and opposite to the load developed on the turbine - the load developed on the device acts along the turbine rotational axis in a positive sense and the load applied to the fluid acts along the same axis but in the negative sense, skewing the wake in the opposite direction to the turbine yaw angle.

The clear agreement with the theoretical approaches noted above was not as strong for the HTI where a more complex wake development was observed for the yawed turbine cases. Initially, the wake is most drastic behind the hub/nacelle and blade tip regions, as noted above, then the position of the maximum deficit meanders to the opposite side of the turbine centre-line (at differing positions for either yaw case) and finally the position of the largest deficit returns to the nacelle-blade combined side creating a curved wake path. The persistence of the merged effect of the hub/nacelle and blade tip extreme was more pronounced in the $\phi = -20°$ case. This finding suggests that ambient turbulence intensity may impact the wake skew under yawed flows; although, as can be seen in Figure 3b, a significant depth wise velocity profile in the HTI case make this finding difficult to generalise.

Figures 7 and 8 show the depth-wise velocity for a horizontal plane through the centre of the turbine hub. In the LTI case the depth-wise velocities recorded show that the wake is rotating in an opposite direction to the turbine rotation as expected, with the centre of rotation shifted to the position of the turbine hub for the $\phi = -20°$ and $\phi = 0°$ cases. However, for the $\phi = 20°$ case the centre of rotation is shifted towards the right hand

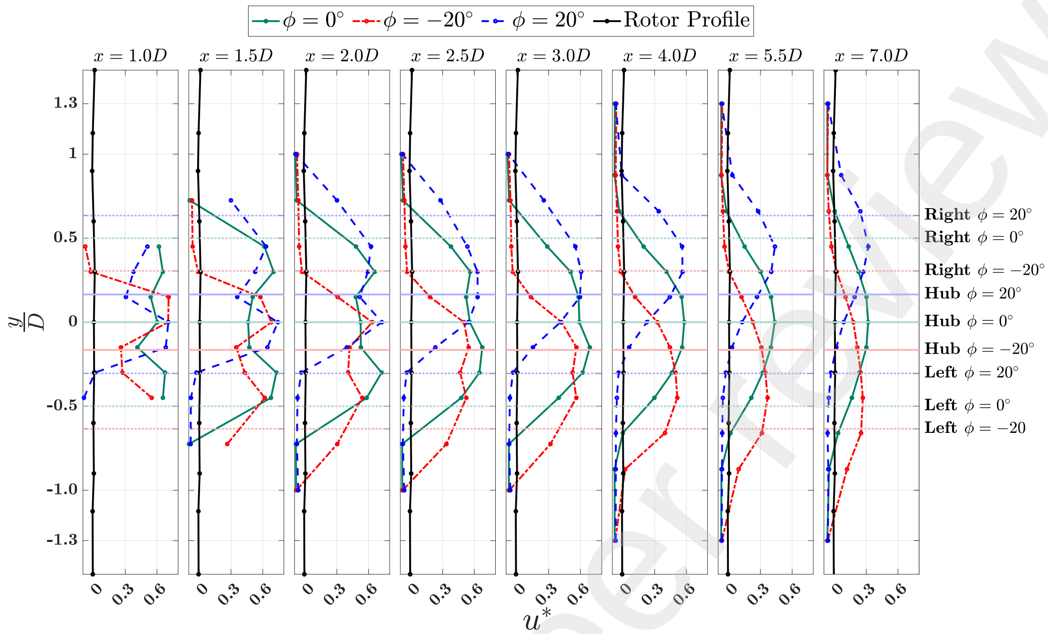

(a) Stream-wise Velocity Deficit, LTI Cases

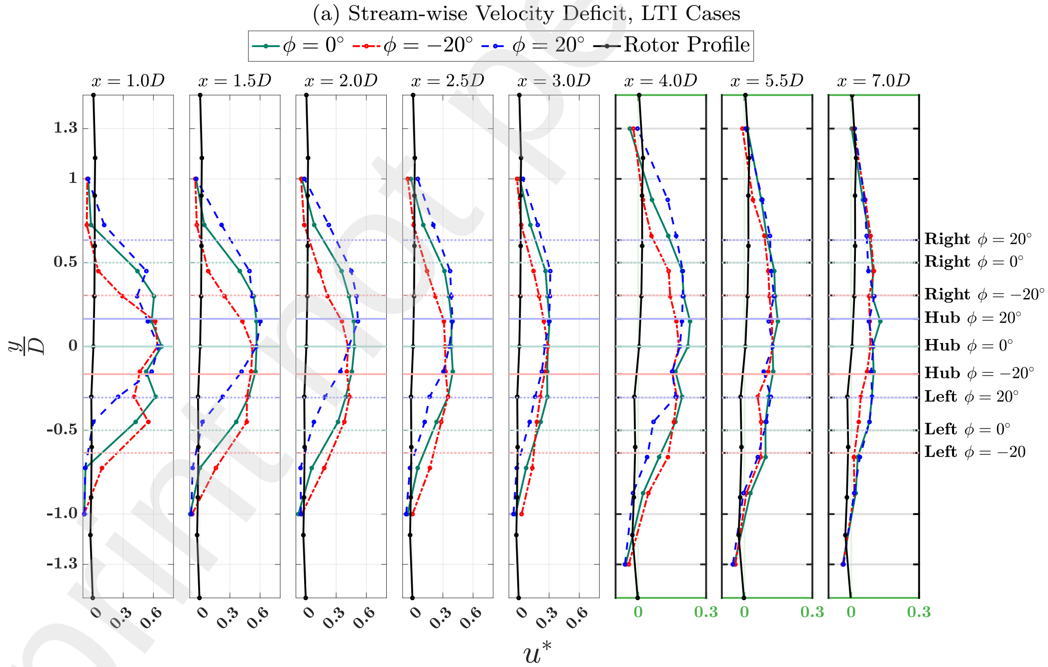

(b) Stream-wise Velocity Deficit, HTI Cases

Figure 5: Time averaged stream-wise flow velocity with downstream and cross-stream position for the (a) LTI cases and (b) HTI cases. NOTE: Coloured x-axis show differing x-limits to better display data.

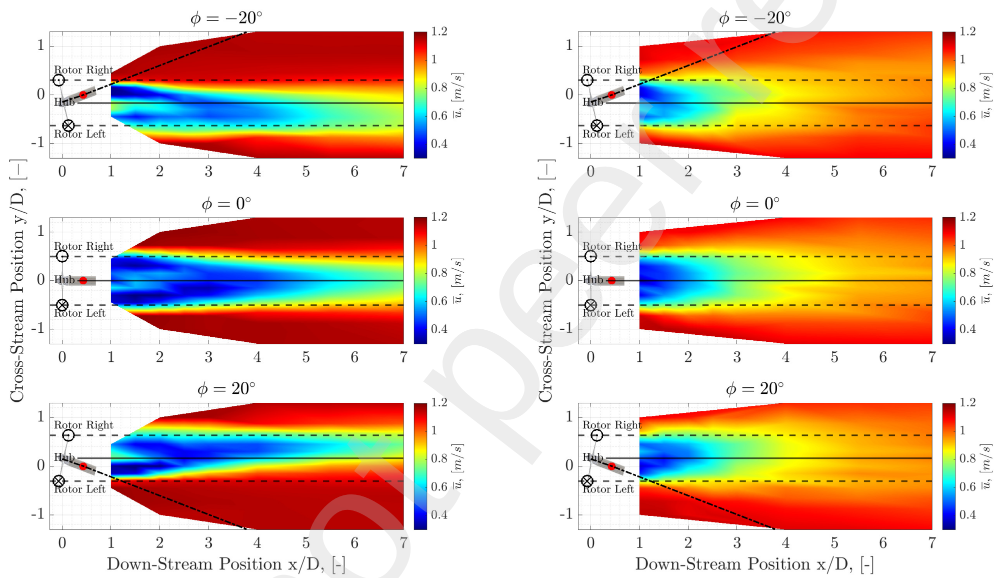

(a) Stream-wise Velocity Wake Map, LTI Cases   (b) Stream-wise Velocity Wake Map, HTI Cases

Figure 6: Time averaged stream-wise flow velocity wake map with downstream and cross-stream position for the (a) LTI cases and (b) HTI cases. Dotted line projecting from the turbine sketch shows the turbine axis.

side of the turbine and shifts increasingly in this direction with downstream distance. In the yawed cases the extent of the induced depth-wise velocity is reduced slightly for the two yawed cases ($\phi = -20°$ and $\phi = 20°$) in comparison to the non-yawed case ($\phi = 0°$).

As shown in Figure 7b, developing a clear picture of the depth-wise velocity generated by the device is difficult due to the inherent rotation in the ambient flow as discussed in Section 2.3. However, in the near wake, at $x/D = 1$, an increased magnitude of depth-wise velocity can be seen. As in the LTI case the opposing direction either side of a centre of rotation, where $w = 0\ m/s$, show that the wake rotates in the opposite direction to the turbine rotation, to a greater degree than the ambient flow. Very quickly, by $1.5 \leq x/D \leq 2$, the depth-wise velocities induced by the rotor are dissipated towards the inherent depth-wise profile observed in the ambient flow. Figure 8 shows that the effect of wake skew can be seen in the depth-wise velocity maps, particularly for the LTI cases.

3.2. Self Similarity and Wake Centre

In this section we consider the structure of the wake from the point of view of its progression and expansion under effective normalisation. Such a manner of viewing wake development is known as a self similarity which, if present, means that the structure of the wake is independent of downstream position when appropriately normalised. Self similarity is well understood for the development of plane wakes behind foundational geometries such as spheres [36], airfoils [37], and disks [38] and we use these formulations with some minor modifications to account for the yawed inflow conditions.

Self similarity has been used previously in the context of tidal energy [39] and is the source of on-going research in the pursuit of improved optimisation of the array structures of tidal farms [34] [40]. The advantage of imposing self similarity on wake development is that the stream-wise velocity field in the wake of tidal stream turbines can be expressed as a set of ordinary differential equations rather than the full Navier-Stokes equations. Such a simplification can be incredibly useful when trying to optimise array structures in realistic channels.

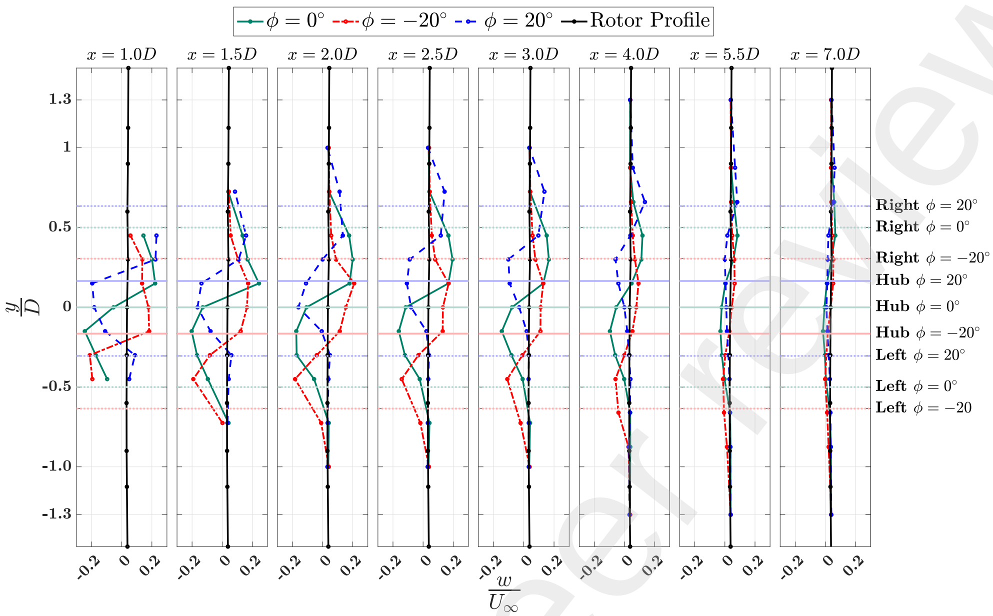

(a) Vertical Velocity, LTI Case

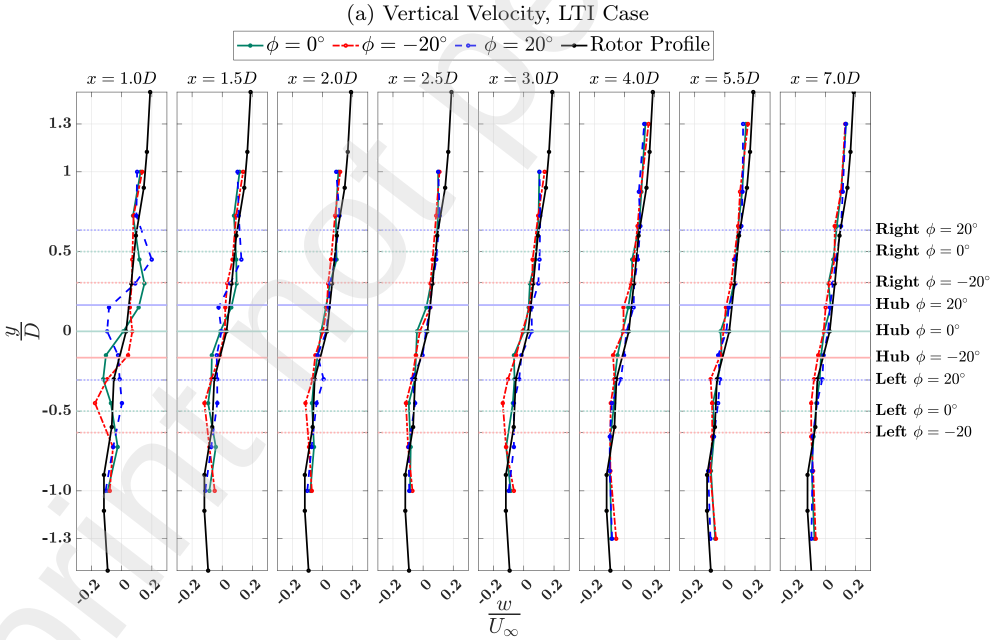

(b) Vertical Velocity, HTI Case

Figure 7: Time averaged vertical flow velocity with downstream and cross-stream position for the (a) LTI cases and (b) HTI cases.

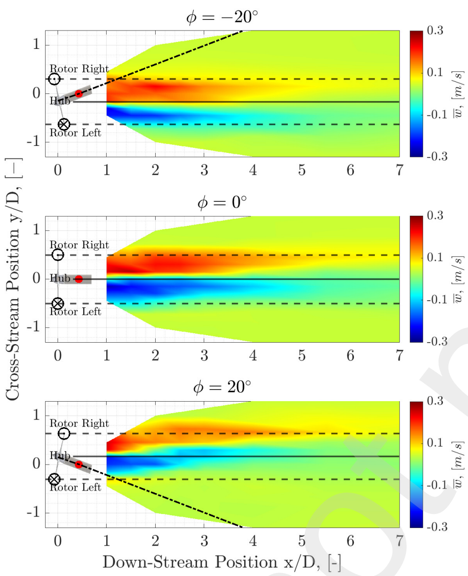

(a) Vertical Velocity Wake Map, LTI Cases

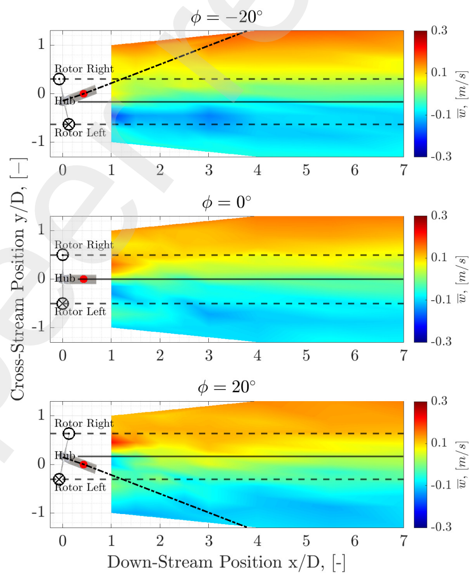

(b) Vertical Velocity Wake Map, HTI Cases

Figure 8: Time averaged Cross-stream flow velocity wake map with downstream and cross-stream position for the (a) LTI cases and (b) HTI cases. Dotted line projecting from the turbine sketch shows the turbine axis.

Here, we consider similarity for the stream-wise velocity field and consider the velocity field at a given horizontal plane (in this case the one vertically aligned with the hub centre). Self similarity is confirmed, if the stream-wise velocity, which is a function of x and y co-ordinates, can be normalized in such a way that it can be written as a function of a single non-dimensional cross-stream co-ordinate ξ.

Equations 10 to 13 show the definitions required to normalise a plane or axisymmetric wake [41]. In Equation 10 the non-dimensional scale parameter, ξ, for the cross-stream position is defined. The parameter is generated by normalising the cross stream position by the distance from the cross-stream position associated with a characteristic velocity deficit to the point where the velocity deficit is half of the given characteristic deficit - Equation 11 defines this characteristic length $y_{\frac{1}{2}}$. In case of axis-symmetric wakes the characteristic deficit is the deficit relative to the stream velocity, u_∞ that occurs at y_{cl} as shown in Equation 12. Finally, we define the self similar velocity deficit in Equation 13, which is purely a function of ξ and has no dependence on x.

$$\xi = \frac{y}{y_{\frac{1}{2}}(x)} \tag{10}$$

$$\overline{u(x, \pm y_{\frac{1}{2}}, 0)} = u_\infty - \frac{1}{2}u_s(x) \tag{11}$$

$$u_s(x) = u_\infty - \overline{u(x, y_{cl}, 0)} \tag{12}$$

$$f(\xi) = \frac{u_\infty - \overline{u(x, y, 0)}}{u_s(x)} = e^{-\alpha\xi^2} \tag{13}$$

In developing a self similar description of the wakes measured, we note that the goal of the analysis is to search for approximate self similarity which may not be observable in the near wake - indeed some studies show consistent self similarity only occurs after $x/D = 8$, [34]. Furthermore, as a novel contribution and particular to yawed inflow, we define y_{cl} using a simple momentum theory treatment of wake development under constant or steady yaw to give an estimate of the wake skew angle and following this the position of y_{cl} utilised in Equation 12. In this regard we use the results from Glauert's analysis of the momentum through an auto-gyro to give the expression in Equation 14 for the wake skew angle [42].

$$\chi = \phi(1 + 0.3(1 - \sqrt{1 - C_T}\ )) \tag{14}$$

The results of this process are presented in Figure 9, where the upper charts show the self similar deficit against normalised cross-stream position for the LTI Cases and the lower charts show the same data for the HTI cases. Each chart is compared with the analytical expression for the self similar deficit as shown on the right hand side of Equation 13.

In both sets of charts the data shows some reasonable adherence to the underlying self similar function given by the right hand side of Equation 13. In the case of the LTI in-flow turbulence setting, it can be seen that the largest deviations from self similarity were in the near to mid wake transects ($< 3x/D$) and in the bypass flow regions. The former statement shows that the wake structure in the near to mid wake region is still dominated by the turbine geometry and therefore y_{cl} is not necessarily the largest deficit recorded as would be the case for purely plane or axisymmetric wakes - this is why we observe values of $f(\xi) > 1$ for portions of these transects. The second statement shows that, as expected and discussed in Section 2.6, the constraints of the recirculating flume have an impact on the self similarity findings outside of the turbine swept area where accelerated bypass flow leads to deviations from the expected curve.

Perhaps surprisingly, relatively good adherence for all yaw angles was observed for mid to far wake transects at the LTI setting. As expected very good agreement with the normal self similar curve was found for the far wake under the $\phi = 0°$ case, particularly for $|\xi| < 1$. In the yawed flow cases there where more deviations from the theoretical curves and the self similar wake showed significant skewing in the bypass flow regions. It was also observed that, the greatest adherence to the theoretical curve was for $x/D = 4.0$ and $x/D = 5.5$ rather than $x/D = 7.0$ as expected - this is likely to show that the wake centre-line deviates from the theoretical position based on the expression in Equation 14.

In the HTI inflow cases, the non-yawed case showed very good agreement with the theoretical self-similar wake shape, other than in the outer regions, again suggesting the impact of the upstream flow characteristics, the blockage effect and the associated bypass flow acceleration. Furthermore, in the no yaw ($\phi = 0$) case the approximate adherence to self similarity was observed for all transects. Similarly, both yawed inflow cases exhibited deviation from the expected curves at value of $|\xi| > 1$ due to the bypass flow.

Interestingly, under both yawed flow cases there is poor agreement or a lack of self similarity for transects in the near wake and far wake, but good agreement or similarity in the mid wake. The authors suggest that this is due to the dominance of the turbine geometry in the flow structure in the near wake and deviation of the wake centre from $y_{cl} = x \times tan(\chi - \phi)$ in the far wake, as predicted by Equation 14.

To study the wake progression in more detail and to understand the regions where self similarity was less consistent, the value of y_{cl} was optimised to give the best adherence to the analytical function given in Equation 13. This was done by searching the cross-stream position to set y_{cl} to give the smallest sum of squared error between the wake measurement points and the aforementioned analytical function. The results of this process are shown in Figure 10. Again the upper charts show the LTI cases and the lower charts show the HTI cases. Under this new approach all cases show a good degree of self similarity for transects in the mid to far wake regions i.e. $x/D > 3$ - with the exception of the points in the outer wake, $|\xi| > 1$, again as a result of the by-pass flow. The development of the centre-line of the wakes, as calculated utilising the momentum theory and via the optimisation described is presented in Figure 11.

Figure 11 shows that the momentum theory predicts that the wakes should have a slightly greater skewed angle for the LTI cases. This increase in the wake skew angle for LTI is resultant from the dependence on C_T in Equation 14 which is higher under the LTI cases - here we note the agreement with other findings where the average C_T value is inversely impacted by the turbulence level in the flow, [27].

The optimised traces immediately show that viewing the wake centre from the point of optimised self-similarity reveals that the extent of the wake progression along the skew angle is curtailed by the bounded flow and resultant

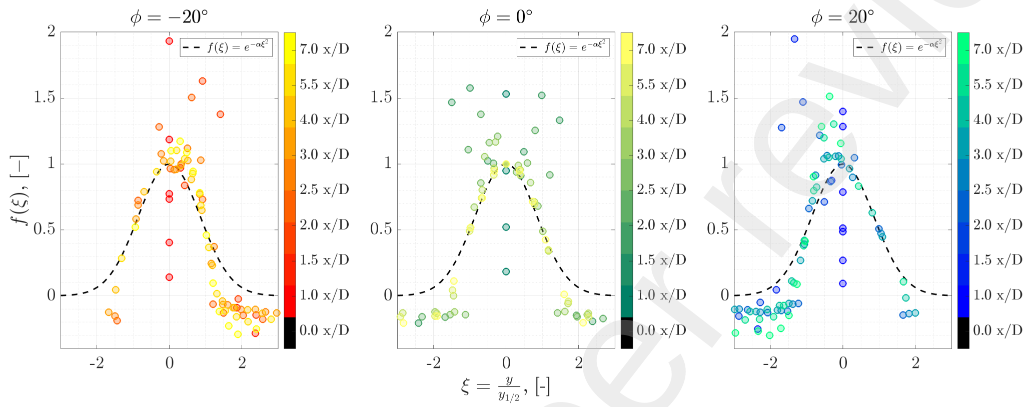

(a) Normalised velocity deficit against normalized wake width, LTI Cases

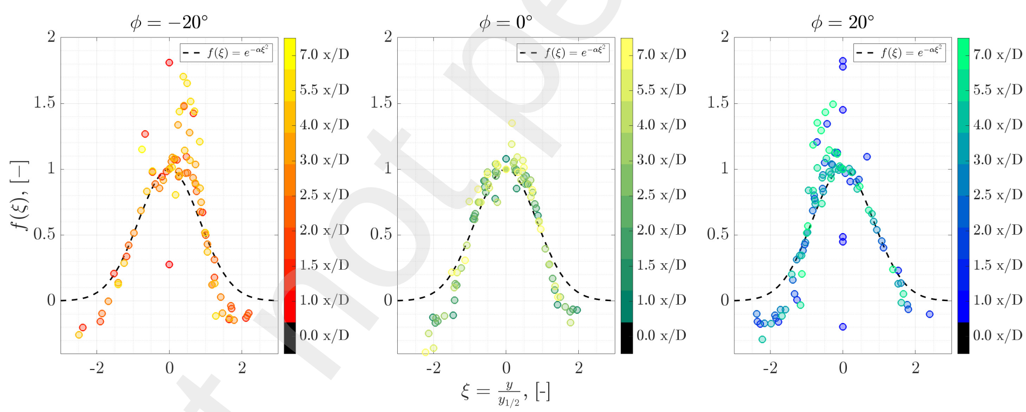

(b) Normalised velocity deficit against normalized wake width, HTI Cases

Figure 9: Self Similar wake parameters for the stream-wise deficit recorded in the wake of the turbine under high and low turbulence intensities, in this case the value of y_{cl} was generated using momentum theory to define the wake skew angle, as detailed in Equation 14.

bypass flow. In the LTI cases, the overall wake progression, after the near wake region, agrees with the theoretical wake centre-line progression in overall direction but not in magnitude. Again for the LTI cases, the wake centre position estimates, generated through the optimisation process, are dependent on downstream position and plateau to a fixed wake offset of $\pm 0.45y/D$. The wake centre line progression calculated via the optimised self-similarity approach shows an overall symmetry about the flume centre under the LTI inflow conditions.

Under the HTI cases a more complex picture was observed via the self similarity optimisation, where the wake centre meanders across the turbine centre in the far wake such that the final position of wake centre line estimated was contrary to the momentum theory position in both direction and extent. In the HTI cases this complexity is compounded by an asymmetry observed between the $\phi = 20°$ and $\phi = -20°$ cases, where in the $\phi = -20°$ case we see the wake centre, calculated via the optimisation, meander across the turbine centre line at a lower downstream position ($\frac{x}{D} = 3$) than the $\phi = 20°$ case ($\frac{x}{D} = 5.5$). Whilst it is not clear why this wake meandering occurs the authors suggest that the impact of the constrained flow is a prominent aspect in "straightening" the wake and potentially reversing its lateral trajectory. The authors also note that an imbalance in the by-pass flow shown in Figure 5, where in the HTI cases, a higher by-pass flow was observed on the left hand side of the rotor. This is most evident in the $\phi = 0°$ plot but can be seen in both the $\phi = 20°$, where the imbalance is exacerbated by the yawed device and the $\phi = -20°$ where the expected symmetry with the $\phi = 20°$ was not observed.

3.3. Turbulent Kinetic Energy and Dissipation Rate

In the following subsection we discuss the nature of the turbulence generated within the turbine wake, the turbulence in the wake will help further mixing of the by-pass flow and has implications for the use of turbulence closure models utilised in CFD.

Firstly we consider the Turbulent Kinetic Energy (k) development in the wake. Turbulent kinetic energy, k, is defined in Equation 15, where the overline signifies taking the time average for a given measurement position as given in Equation 1. The balance of the kinetic energy of the turbulent fluctuations induced by the turbine rotor, as described by the value k, is

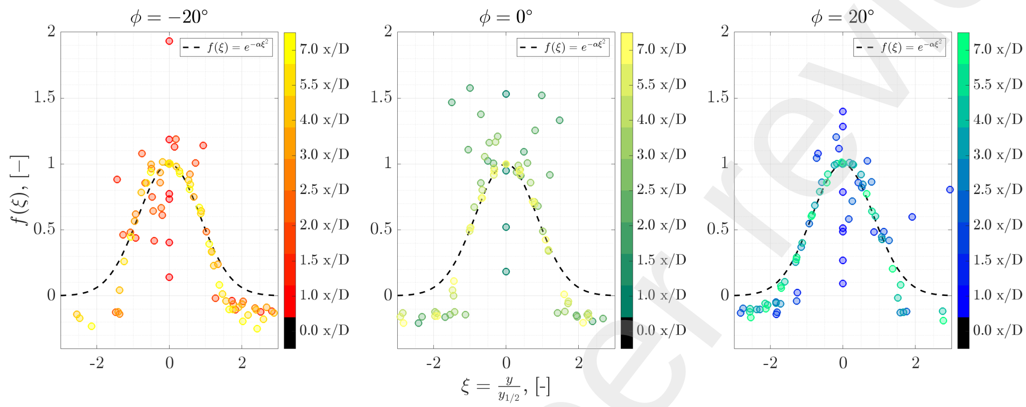

(a) Normalised velocity deficit against normalized wake width, LTI Cases

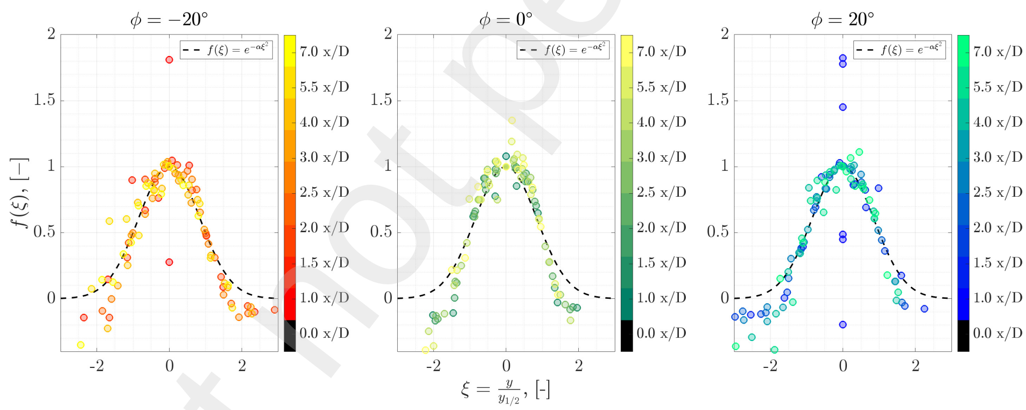

(b) Normalised velocity deficit against normalized wake width, LTI Cases

Figure 10: Self Similar wake parameters for the stream-wise deficit recorded in the wake of the turbine under high and low turbulence intensities, in this case the value of y_{cl} was generated using by minimising the sum of squared error between the theoretical value of $f(\xi)$ and the measured values.

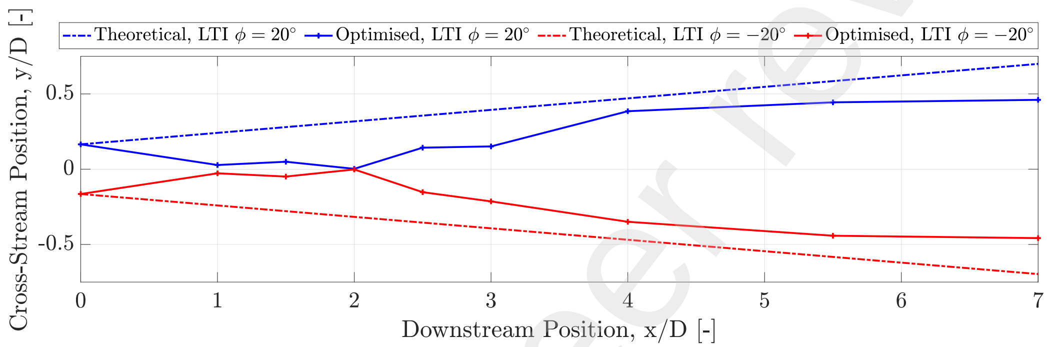

(a) LTI Cases

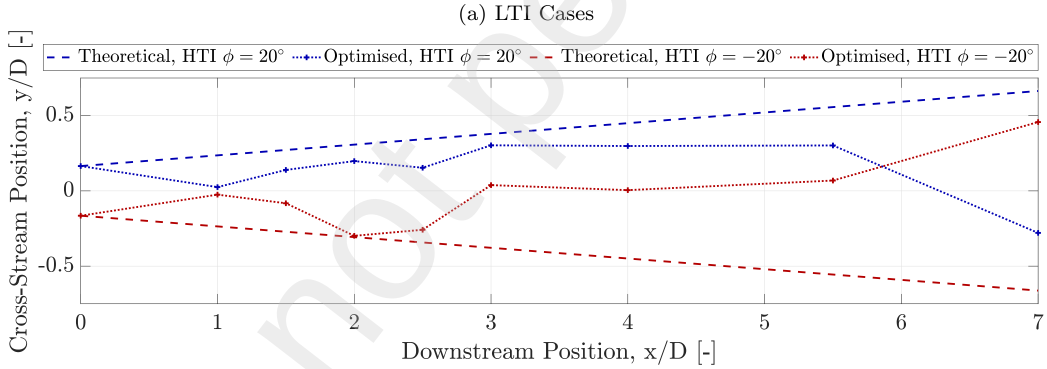

(b) HTI Cases

Figure 11: Chart showing the wake centre-lines as calculated using the momentum theory and by optimising the adherence of the wake to the self similar function $f(\xi) = e^{-\alpha\xi}$.

crucial to understanding the physical processes in the wake and particularly important in turbulence modelling. Figure 12 shows the turbulent kinetic energy, k, measured via the 3-component 3D LDV for each of the cases tested, Figure 12a shows the LTI cases and Figure 12b shows the HTI cases - where k is shown with cross-stream position (y/D, x-axis) and downstream position (x/D, plot colours).

$$k = \frac{1}{2}\overline{(u'^2 + v'^2 + w'^2)} \tag{15}$$

Figure 12a shows the measured k for each LDV measurement position and yaw case, immediately apparent, and unsurprisingly, the turbine rotor is converting energy from the inflow to turbulent energy in the wake which is not fully dissipated by $x/D = 7$ - as seen by comparing the black trace to coloured traces. In the near wake, $x/D = 1$, the highest level of k is not reached meaning there is further turbulence production moving downstream of the rotor. In this region ($1 \leq x/D \leq 1.5$) the peak level of turbulent kinetic energy produced was dependent on the yaw angle and peak k values of 0.035 m^2/s^2 , 0.047 m^2/s^2 and 0.070 m^2/s^2 were observed for the yaw cases, $\phi = -20°$, $\phi = 0°$ and $\phi = 20°$, respectively. In this region the early wake appeared to be dominated by the merged effects of the nacelle and shadowed blade-tip as discussed in Section 3.1 - the aforementioned peaks in k values occur between the hub and right blade for the $\phi = -20°$ case, between the hub and left blade for the $\phi = 20°$ case and finally directly behind the hub for the $\phi = 0°$ case. It should be noted here that the reduced set of measurement positions for the LTI cases may have meant increases in k due to high shear regions around blade tips which may have been missed in this near wake region - particularly for the $\phi = 0°$ case, where no increase in k at the blade tip regions was found.

Further downstream, the k in the wake is highest in the high shear regions as expected, this resulted in three peaked regions at the hub/nacelle and blade tips (left and right) for the $\phi = 0°$ case. The peaks associated with the right blade and the nacelle for the $\phi = -20°$ case are merged as were the peaks associated with left blade and the nacelle for the $\phi = 20°$ case. In each of the yaw cases the k value associated with the non-shadowing blade position at $x/D = 1.5$ exhibited the highest k value - this peak was dissipated or diffused by $x/D = 2$. In each of the yaw cases the turbulent kinetic energy distribution is asymmetric with the position of the blade peaks moving from outside the turbine radius towards the respective blade tip positions (left:

$\phi = -20°$ & right: $\phi = 20°$). Finally, at $x/D = 7$ slightly higher peak turbulent kinetic energy was observed for the no yaw case, relative to the yawed cases.

Figure 12b shows that in the HTI case the turbine also converted some of the energy in the free stream flow into turbulent kinetic energy and in the HTI case this energy was found to have mostly dissipated by $x/D = 7$ - albeit towards a higher ambient k-value than the LTI cases, as expected. In the near wake, $x/D < 2$, the peaks associated with the higher shear regions created by the blade tips and hubs/nacelles can be seen, along with the aforementioned merging of the shadowed blade tip and hub/nacelle effects in both yawed cases, these effects are dissipated by $x/D = 4$ in all cases. The generally higher levels of k, observed for the HTI cases, coincides with the findings that the effects of shear structures and vertices are broken down at a faster rate when the ambient or free stream turbulence is higher. Finally, whilst the obvious structures associated with the blade tip regions and nacelle are broken down more quickly in the HTI case, there is an overall asymmetry in the turbulence kinetic energy introduced by yawing the turbine. These asymmetries were found to persist for all downstream positions measured. For each yaw case, k was asymmetric in the sense of higher relative k values observed in the wake of the combined nacelle and blade extreme position - i.e. $y/D = 0.3$ in the $\phi = -20°$ case and $y/D = -0.3$ in the $\phi = 20°$ case.

Closely related to the level of turbulent kinetic energy, k, throughout the wake is the rate at which turbulence is converted to heat through molecular interactions - the turbulence dissipation rate ϵ. Generally, experiments have shown that ϵ is correlated to the k - indeed frequently it is considered that the rate of turbulence production is equal to the rate of turbulence dissipation for turbulent flows in equilibrium [43] [44]. Furthermore, assumptions on the nature and transport of both k and ϵ are utilised in CFD models to generate relationships for closing the Navier-Stokes relationships, for example in the commonly used k-ϵ approach to modelling turbulence which is very popular in modelling tidal stream devices [44].

The turbulence dissipation rate, ϵ, is calculated from LDV measurements by assuming the turbulence spectra measured are of the form $C_0\mathcal{K}^{\beta}$, as shown by the approximate relation in Equation 16. Here, $\mathcal{K}$ is the wave number given by $\mathcal{K} = \frac{2\pi}{l}$, where l is an arbitrary length scale of the turbulent flow and in the case of the spectra proceeds from larger length scales to smaller length scales with increasing $\mathcal{K}$ - in this case the wave number index for the spectra were generated using Taylor's hypothesis that motion of each length

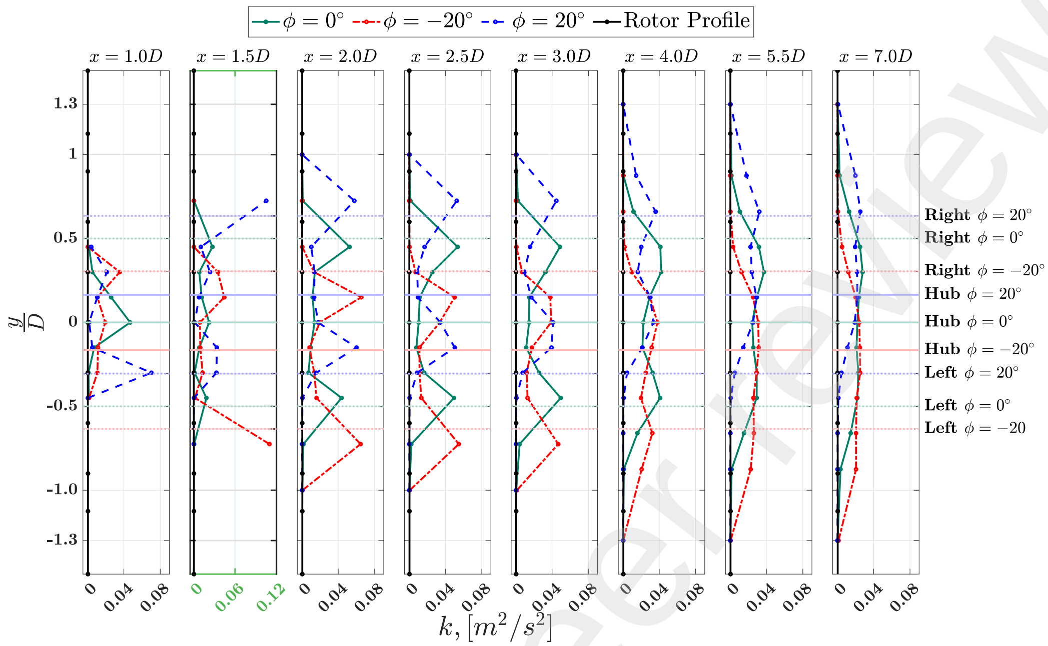

(a) Time-Averaged turbulent kinetic energy recorded for the LTI Cases

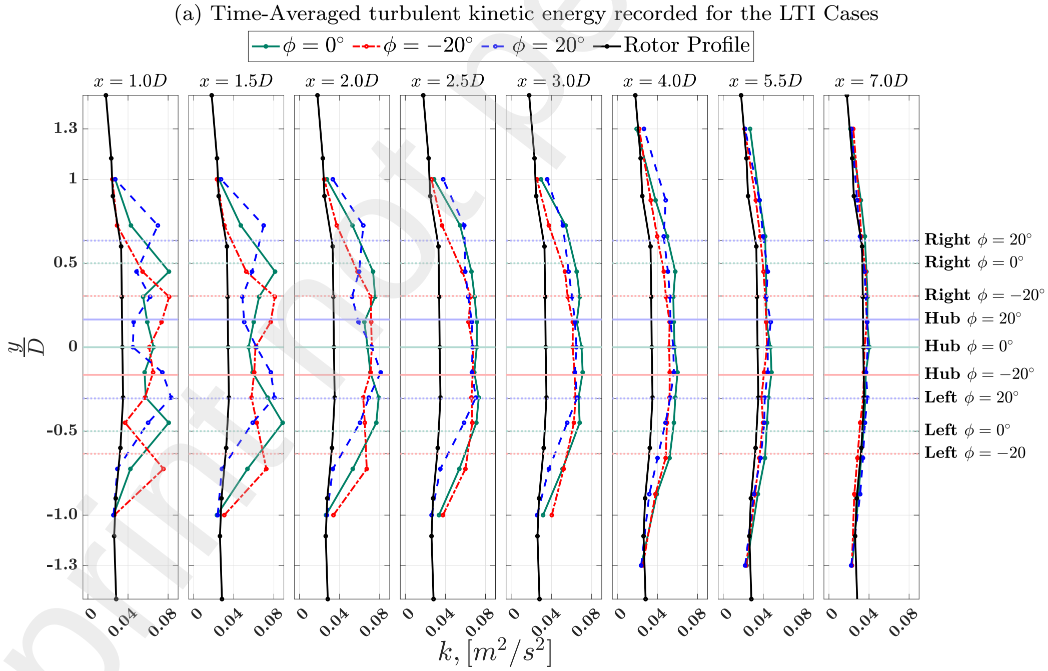

(b) Time-Averaged turbulent kinetic energy recorded for the HTI Cases

Figure 12: Turbulent kinetic energy, k, with downstream and cross-stream position for the (a) LTI cases and (b) HTI cases.

scale past a given point is driven by the global average flow velocity, $\overline{U_\infty}$. This gives $\mathcal{K} = \frac{f}{\overline{U_\infty}}$, where f is the standard frequency index for a developed spectra.

Then, using least squares regression the assumed function, $C_0\mathcal{K}^\beta$, is fitted to the data in the inertial range portion of the spectra yielding an estimate of C_0 assuming $\beta \approx -5/3$. The spectrum is related to ϵ by Kolomogoroff's 2nd similarity hypothesis, which states that statistics of motions on scales within the inertial subrange are uniquely determined by ϵ. Such a hypothesis is expressed by the equality in Equation 16, where C = 1.5 as observed in experiments [45][46]. The right hand side of Equation 16 can be equated to the fitted form of the spectra using the value of C_0 generated through the least square regression and rearranged to give an estimate of ϵ given by Equation 17.

$$E(\mathcal{K}) \approx C_0\mathcal{K}^\beta = C\epsilon^{2/3}\mathcal{K}^\beta \tag{16}$$

$$\epsilon = \left(\frac{C_0}{C}\right)^{3/2} \tag{17}$$

Figure 13a shows the relationship between k and ϵ and downstream position for the wake measurements made at LTI, whereas Figure 13a shows the same relationship for the HTI case. Figure 13a shows a reasonable correlation between the observed k values and the estimated dissipation rate, ϵ, as expected. In the near mid-wake the correlation is a little steeper indicating higher dissipation rates in regions in close proximity to the turbulence generated by the turbine rotor, for these cases there were also slight variations between the yaw angle cases with a particularly steep gradient observed for the $\phi = 0°$ case. In the far wake very similar results were observed across all cases and generally there was a reduction in the correlation between the turbulent energy and dissipation level in the flow with both tending towards zero for the transects measured furthest downstream.

Figure 13b, again, shows a clear correlation between turbulent energy and dissipation, this relationship is consistent for the far wake measurements ($\frac{x}{D} > 4$) and shows a minimal level of turbulent dissipation, inline with the turbulence generated by the overall flow regime. In the near to mid wake region ($1 < \frac{x}{D} < 4$) a non-linear relationship develops. In the $\phi = 0°$ case there is an almost asymptotic relationship whereby small increases in turbulent energy result in large increases in dissipation rate, showing the local

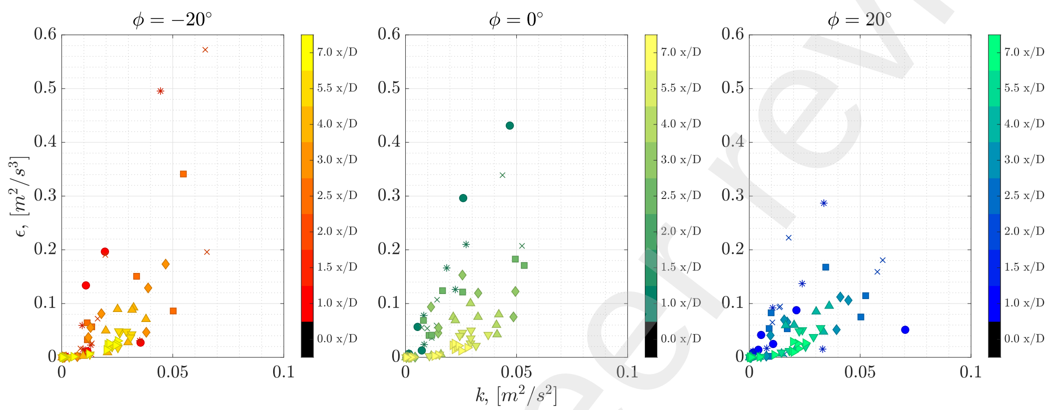

(a) Turbulence Dissipation Rate, LTI Case

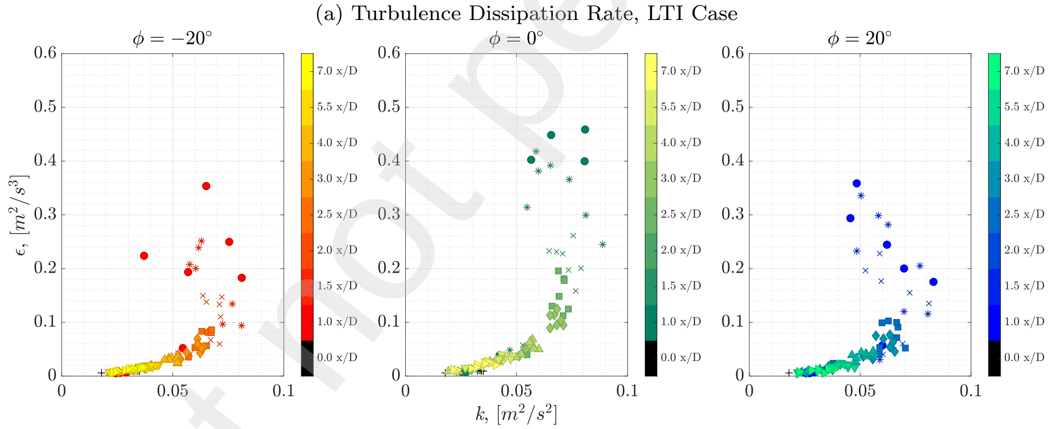

(b) Turbulence Dissipation Rate, HTI Case

Figure 13: Turbulent energy dissipation rate, ϵ, with downstream and cross-stream position for the (a) LTI cases and (b) HTI cases.

adaptation of dissipation to maintain equilibrium. The highest dissipation rates were observed in the $\phi = 0°$ case. Accompanying the lower dissipation rates observed in the yawed inflow cases, are regions of high dissipation rate with relatively low turbulent energy, creating an almost inverse trend - it is not clear why this relationship develops but it is potentially caused by a lack redistribution of turbulent energy via diffusion or convection. Finally, the authors note the broad adherence within the figures to a polynomial form which may be related to an expression that can be developed via dimensional considerations relating, k and ϵ - such an expression is given in Equation 18, where ν_T is the eddy viscosity which to generate the expression it is assumed that, $\nu_T = f(\epsilon, k)$.

$$\epsilon = \frac{C_\mu}{\nu_T} k^2 \tag{18}$$

This finding is more clearly adhered to at greater distances downstream of the turbine. where as one moves downstream the return to isotropic turbulence can be observed. Clearly then, the geometric structures associated with the turbulence generated via the turbine rotor are broken down, when moving away from the turbine rotor.

3.4. Integral Length Scale

To further integrate the structure of the turbulence generated in the turbine wake, an assessment of the integral length scale, denoted as $\mathcal{L}$, linked to the stream-wise velocity fluctuations was conducted. This analysis aimed to gain insights into how the large-scale turbulent structures evolved with cross-stream and downstream position.

Figure 14a and 14b shows the $\mathcal{L}$ for the LTI and HTI cases, respectively for each of the yaw cases. In the LTI case, Figure 14a, a clear reduction in length scale can be viewed in the near wake which is of a similar size ($\mathcal{L} < 0.1m$) for each of the yaw cases. The length scale then grows with downstream distance to $\mathcal{L} \approx 0.2m$ at $\frac{x}{D} = 7.0$, where the length scale remains significantly smaller than observed upstream of the turbine. Here, the consistent growth of turbulence length scale with downstream distance is in agreement with other similar studies and shows the complex interaction of unfurling vortical structures, the inertial sub-range where eddies are broken down and the ultimate destruction of smaller eddies via viscous dissipation. In the bypass flow, ($-0.5 < \frac{y}{D} > 0.5$), length scales of a similar size $0.5 < \mathcal{L} < 1$ can be observed.

Under the HTI cases, a reduction in length scale can be seen in the transects below $\frac{x}{D} = 2$, where in the $\frac{x}{D} = 1.0$ transects, length scale in the region of $0.25m$ were observed. The higher ambient turbulence throughout the flow has sped up the elongation of measured lengths scale via more rapid unfurling and mixing of larger flow structures. Very quickly a chaotic picture ensues with lengths scales in the order of the those found at the rotor plane, this is true for all yaw cases after $\frac{x}{D} > 2.0$.

3.5. Turbulence Isotropy

The final aspect of the analysis presented is to consider the anisotropy of turbulence in the wake under the influence of yawed inflow at the LTI and HTI test cases. The anisotropy is studied here utilising the 'Lumley Triangle', developed by Choi and Lumley [47], which has been utilised in the description of the turbulence in the wake of HATTs previously [12][48][49]. Anisotropy, can show the presence of coherent structures in turbulent flows [50] and has an impact on the turbulence methods utilised within CFD models which often assume isotropic turbulence [12]. Understanding the return to isotropy under the test cases measured will help develop an understanding of how to appropriately model turbulence in the wake of HATTs and on the propagation of coherent structures such as tip vertices.

The turbulence triangle is derived by considering the anisotropy of the Reynolds stresses, $\overline{u_i'u_j'}$, which can be characterised via the anisotropy tensor, b_{ij} given by Equation 19, where k is defined as shown previously in Equation 15 and the indices i and j indicate differing Cartesian directions x, y, z associated with the velocity components (u,v,w) and finally, δ_{ij} is the Kronecker delta where $\delta_{ij} = 1$, if $i = j$ and $\delta_{ij} = 0$, otherwise. Here, b_{ij} is a 2^{nd} rank tensor, which is symmetric and has zero trace and tends to zero when turbulence becomes isotropic [47]. The anisotropy tensor being of rank 2, has a set of three principle invariants which by definition do not change under a change of basis, these invariants (I, II, and III), are defined in Equation 20, where λ_1, λ_2 and λ_3 are the eigenvalues associated with the eigenvector-eigenvalue decomposition of the anisotropy tensor.

These invariants can then be utilised to define the boundaries of the turbulent triangle via variables ξ and η defined in Equation 21. Figure 15, adapted from [49], shows how the values of ξ and η can be interpreted. The curved 'base' of the Lumley triangle adheres to the following non-linear relationship, $\eta^2 = 1/27+2\xi^3$ and shows where turbulent structrues become 2-dimensional tending towards 1-dimensional at $\eta = \xi = 1/3$. Moving from the

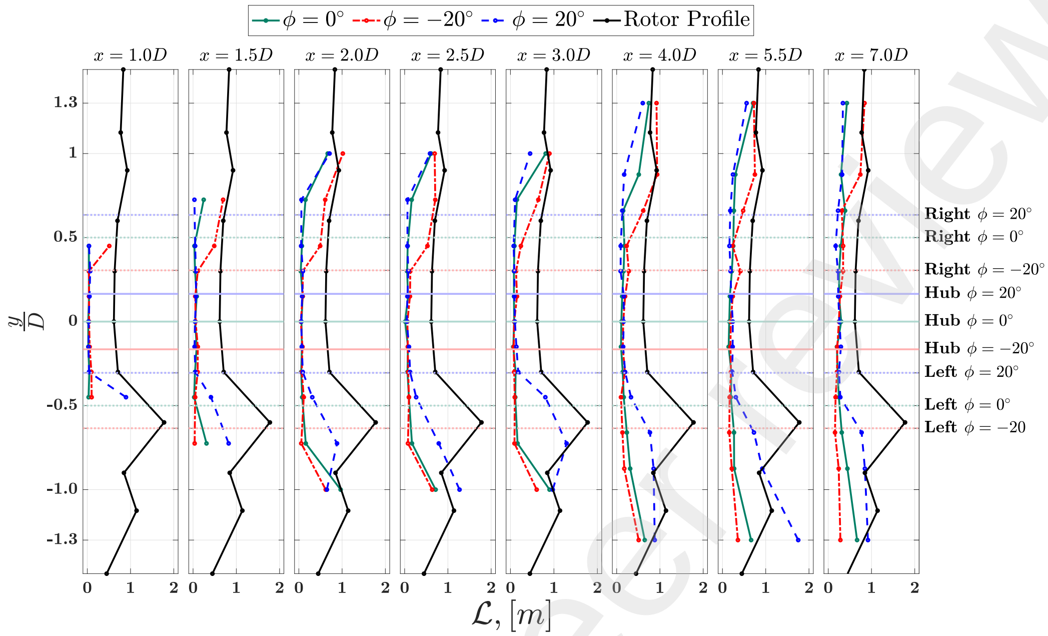

(a) Integral Length Scale, LTI Case

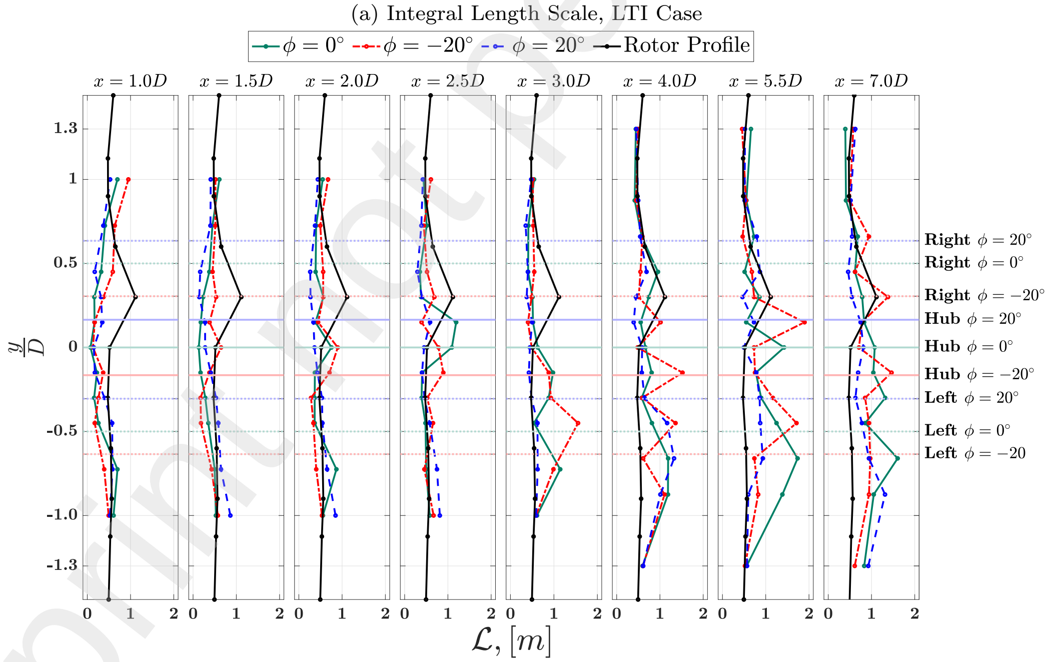

(b) Integral Length Scale, HTI Case

Figure 14: Integral length scale, $\mathcal{L}$, with downstream and cross-stream position for the (a) LTI cases and (b) HTI cases.

origin, the sides of the triangle show axisymmetric turbulence where $\xi = -\eta$ (tending towards oblate or squashed) and $\xi = \eta$ (tending towards prolate or elongated structures).

$$b_{ij} = \frac{\overline{u_i' u_j'}}{2k} - \frac{1}{3}\delta_{ij} \tag{19}$$

$$\begin{aligned} I &= 0 = \lambda_1 + \lambda_2 + \lambda_3 \\ II &= \frac{-b_{ij}b_{ji}}{2} = \lambda_1^2 + \lambda_1\lambda_2 + \lambda_2^2 \\ III &= \frac{b_{ij}b_{jk}b_{ki}}{3} = -\lambda_1\lambda_2(\lambda_1 + \lambda_2) \end{aligned} \tag{20}$$

$$\begin{aligned} \xi^3 &= \frac{III}{2} \\ \eta^2 &= \frac{-II}{3} \end{aligned} \tag{21}$$

Figures 16a and 16b show the Lumley triangles for the wake measured under each condition. In the LTI case the inflow turbulence is minimal and can be seen to have a prolate spheroid shape tending towards 2-D axisymmetric turbulence. The effect of the rotor was to generate oblate spheroid structures which were not present in the flow at the rotor plane prior to installation. No clear trajectory towards isotropic turbulence can be observed and with downstream distance from the rotor one can see the flow tends towards 2-D asymmetric elongated turbulent structures as observed prior to turbine installation - however this tendency is not consistent across the differing yaw cases. The finding would suggest that the inlet turbulence requires far greater mixing to developed isotropic turbulence at the inlet to the rotor.

Under the HTI case (Figure 16b) a more clear trajectory tending towards isotropic turbulence was observed with downstream distance, however perfect isotropic turbulence was not observed, neither prior to installation or in the far wake. In the $\phi = -20°$ case the yawed rotor has generated clearly 2-D axisymmetric elongated turbulence which is dissipated with downstream position. Similar structures were introduced by the rotor in the $\phi = 0°$ case and the $\phi = 20°$ case but not to the same degree. In all instances a minority of measurement positions exhibited 2-D axisymmertic structures of the oblate

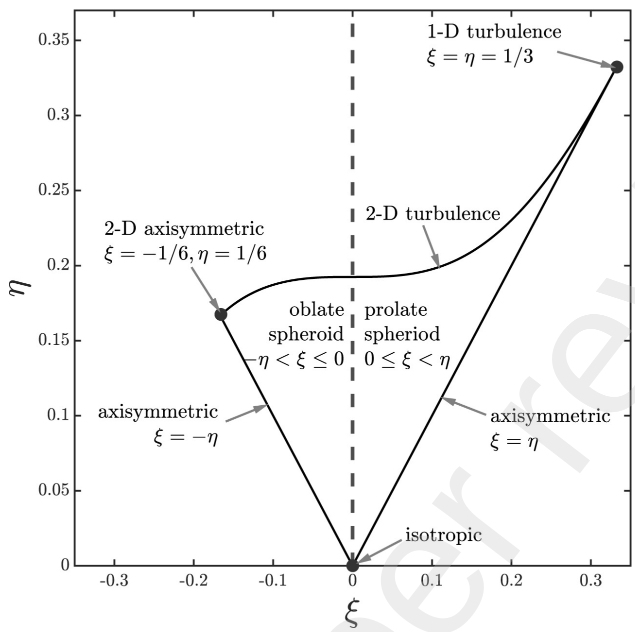

Figure 15: Schematic of the interpretation of the Lumley triangle utilised to analyse the shape of the turbulent structures in the wake of the HATT. [49]

spheroid shape, this was more pronounced in the $\phi = 0°$ and $\phi = 20°$ cases. As expected, due to observations in [12] [48] and [49], in the near wake elongated axis symmetric turbulence is generated by the rotor. Again, inline with previous studies no fully isotropic turbulence was observed by $x/D = 7.0$. However, the authors note the varying levels and characteristics of the anisotropy observed between the three experiments and those presented here, suggesting that the inflow characteristics do have an impact on the findings.

To understanding in more detail the return to anisotropy, Figures 17 and 18 show the principle values of the anisotropy tensor, b_{ii} - the upper charts shows the values inline with the rotor right side, the central charts show the values inline with hub and the lower charts show the values aligned with the left side of the rotor. The principle values show the degree of anisotropy in each principle direction (x, y and z) and sum to zero, as the trace of the anisotropy tensor is zero - Equation 20. Figures 17 and 18 show comparable values to both [47] and [48]. We immediately see that the development of the anisotorpy with downstream position in the turbulent wakes is a function of inflow conditions (difference between Figures 17 and 18), cross-stream position (difference between upper, middle and lower charts) and yaw angle

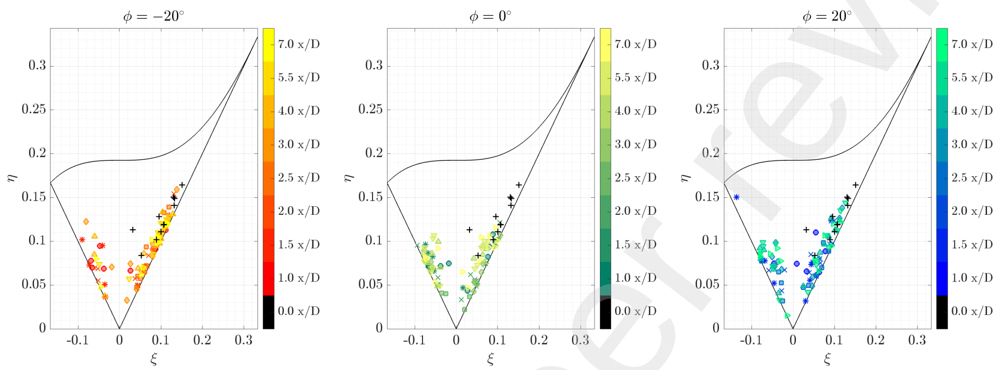

(a) LTI Case.

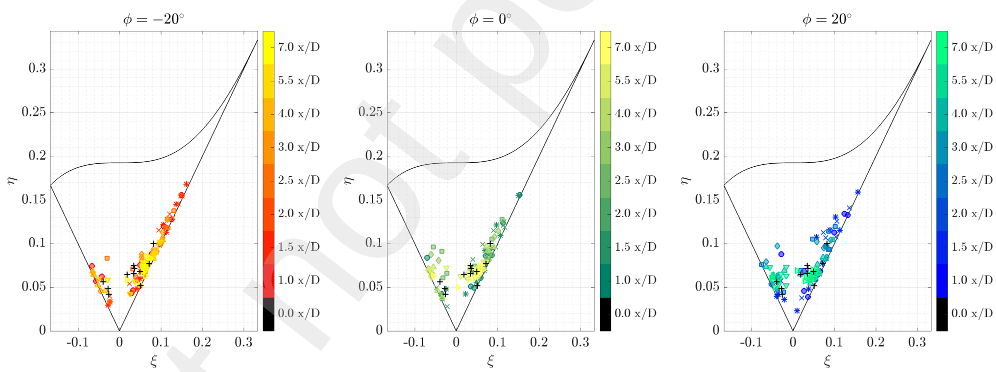

(b) HTI Case.

Figure 16: Lumley triangles showing anisotropy of turbulence structures with downstream position.

(difference between differing coloured markers).

Generally, the trajectory of the principles of the anisotropy tensor are rather chaotic, this is particularly true under the LTI cases. Under the LTI cases, each principle axis shows significant levels of anisotropy and one can only roughly observe the tendency for each principle value to converge to a fixed level with downstream position. Under the HTI cases more clear trajectories can be observed - each principle value seems to converge to a given level. Furthermore, in the HTI case the third principle, b_{33} (z-direction), has a markedly smaller level than b_{11} and b_{22}.

Whilst the variations in the figures are rather chaotic, there is consistency across both inflow conditions for the $\phi = 0°$ cases - here, the data at either blade extreme is similar across each principle direction (upper and lower charts are similar for all three lateral charts), suggesting a level of symmetry about the rotational axis. This is in contrast with the principle values recorded behind the hub and nacelle (central row of charts) which interestingly show almost opposite tendencies to the blade extremes (this is particularly clear in Figure 18).

In the $\phi = -20°$ and $\phi = 20°$ cases, very similar trajectories for the anisotropy in all principle directions was observed behind the hub. Whereas almost inverted roles were observed at the blade extremes - i.e. for b_{11} (x-direction) the upstream blade generates a greater level of anisotropy such that in the upper charts for $\phi = -20°$ higher values were observed and the opposite in the lower charts.

4. Conclusions

This paper has discussed measurements of the flow velocity in the near to mid wake of a HATT under laboratory conditions utilising the re-circulating flume at IFREMER, Boulogne-sur-Mer, France. A 3D LDV system was used to take point measurements of the flow at a pre-configured series of positions in the turbine wake. Here we analyse the wake structure in the horizontal plane aligned with the turbine rotor. The wakes were measured for three turbine yaw angles as defined in Figure 2 for two differing TI inflow settings.

The flow velocity deficit in the stream-wise direction showed that indeed the yawing of the turbine introduced a skewed wake. In the LTI cases marginally faster recovery was observed for both the yawed cases but this was not observed in the HTI cases. The rate of wake recovery was significantly higher in the HTI cases than in the LTI cases which is inline with

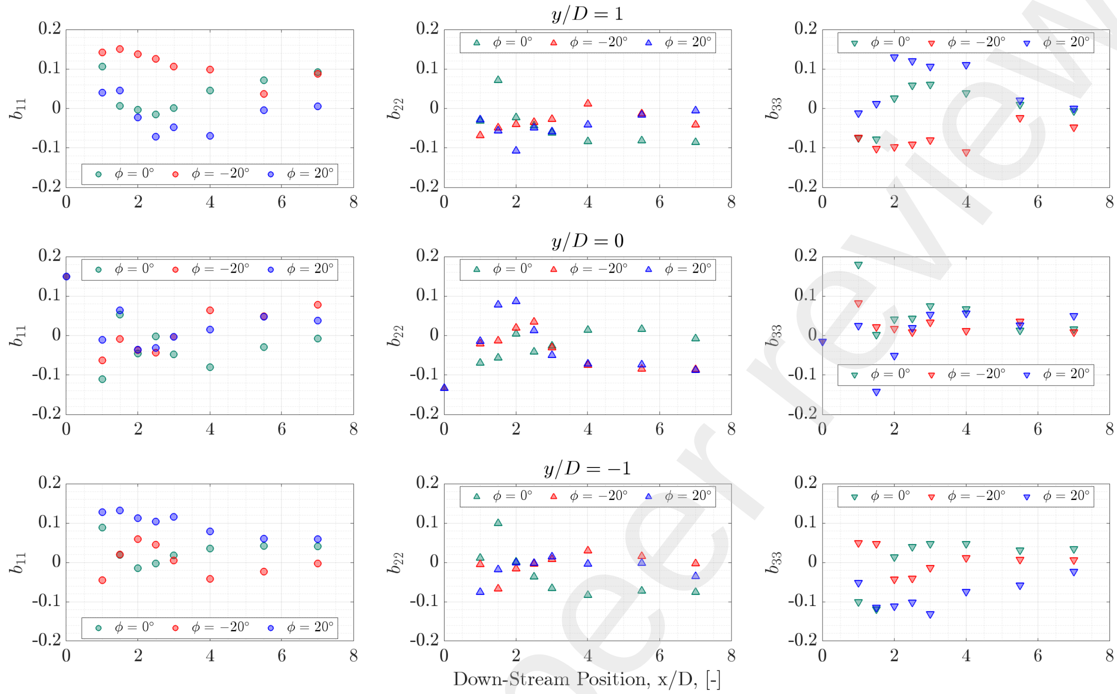

Figure 17: Lumley triangle showing anisotropy of turbulence structures with downstream and cross-stream position for the LTI cases.

other findings. The degree of deficit in the wakes observed was inline with other experimental results also [12][9][48]. Consideration of the vertical velocity induced by the rotor, structures similar to Rankine or Lamb-Oseen [51] vortexes were observed, these were particularly clear for the LTI but were obscured by a flume wide vorticity which masked these findings for measurement positions $x/D > 1.5D$ in the HTI case.

A degree of self similarity was observed for all wakes when combining self-similarity theory and skew angle predictions developed by Glauert [42]. The self similarity curves generated were generally very consistent for the no yaw cases ($\phi = 0°$) under both TI settings. Under the yawed cases the inclusion of the skew angle in setting the reference velocity for each transect facilitated a self similarity analysis of the skewed wakes which gave reasonable results. An optimisation was performed to improve the adherence to the self similar wake shape by selecting the wake centre-line (and reference) position (and value) that gave the best agreement to the aforementioned wake shape. This approach gave a method of inspecting the wake centre-line with downstream position which was compared with the skewed wake centre predicted by Glauert. This process uncovered a complex picture showing wake meander - in some cases across the hub centre - but ultimately showed that the inability of the wake to fully expand, due to the flume walls, had a significant impact on the results. Even so, some evidence wake skewing and bending was observed and could be useful in array power output optimisations. However, further work is required in this regard, this work should either be undertaken numerically or by conducting tests with a smaller blockage ratio.

The turbulence in the wake was analysed in terms of energy levels, k, length scale, $\mathcal{L}$, and anisotropy. The levels of turbulent kinetic energy in the wake k, were clearly elevated by the turbine and peaks in k were observed aligned with blade extremes. Interestingly, the peaks were larger for the

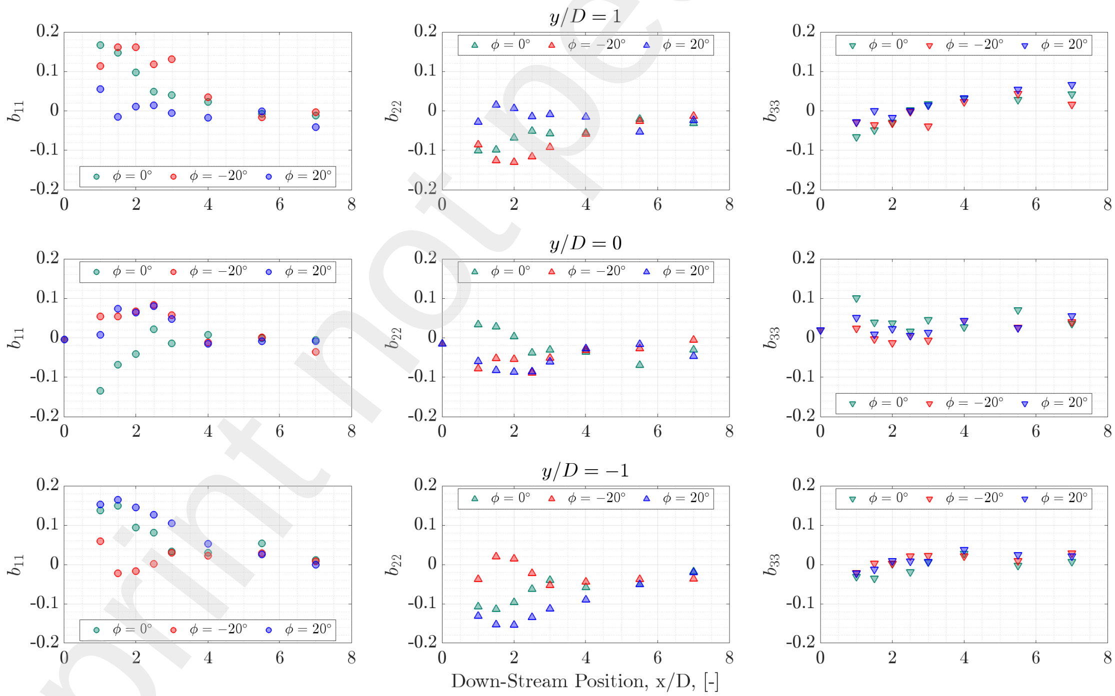

Figure 18: Lumley triangle showing anisotropy of turbulence structures with downstream and cross-stream position for the HTI cases.

LTI case than the HTI case with these high peak values only observed in the yawed turbine cases. In all cases the peak levels of k increased between $1D$ and $1.5D$ downstream of the turbine. The coherence of high levels of k aligned with the blade extremes and the hub dissipated more slowly under LTI inflow and quickly under HTI inflow. The relationship between, k and dissipation rate ϵ was also explored and showed that in the mid wake a parabolic relationship was observed but this was not the case in the near wake. The parabolic relationship was observed after $x/D = 5.5$ and $x/D = 2.0$ for the LTI and HTI cases, respectively. This relationship was consistent across all yaw settings and can be developed from dimensional reasoning [43].

Analysis of the length scales of the turbulent structures in the wake showed evidence that the turbine generated smaller structures than the ambient inflow. In the HTI cases these smaller structures grew quickly to sizes similar to the inflow turbulence. In the case of the LTI inflow the smaller structure persisted for longer and full growth to the inlet scales was not observed. Growing length scales in HATT wake turbulence has been observed previously and our study supports these findings.

The presence of the turbine also changed the anisotropy of the turbulence - the observed changes were sensitive to the level and type anisotropy observed in the inflow. Changes in the anisotropy in the LTI cases was chaotic and a return to elongated 2-D axisymmetric structures, observed in the inflow, was not clearly observed - this was further observed in the chaotic traces of the anisotropy tensor principle values. More consistent development of the tensor invariants and the principle values were observed in the HTI cases.

This work showed the complexity of the wake development and the potential for wake skewing and bending which maybe useful in array optimisation. The turbulence within the wake is complex and dependent on the inflow turbulence and its structure as well as the control strategy of the rotor, in this case speed control. This latter point needs further investigation and may well give some insight to some of the effects discussed.

Acknowledgements and Funding

- This work was supported by the Engineering and Physical Sciences Research Council [DyLoTTA – EP/N020782/1];
- Facility access for this work was funded by MARINET2 as part of European Union's Horizon 2020 research and innovation programme under grant agreement No 731084.

Data

The data underpinning this article can be accessed at: https://doi.org/10.17035/d.2020.01242874

References

[1] C. H. Frost, P. S. Evans, M. J. Harrold, A. Mason-Jones, T. O'Doherty, D. M. O'Doherty, The impact of axial flow misalignment on a tidal turbine, Renewable Energy 113 (2017) 1333–1344. doi:10.1016/j.renene.2017.07.006.

[2] A. Bahaj, A. Molland, J. Chaplin, W. Batten, Power and thrust measurements of marine current turbines under various hydrodynamic flow conditions in a cavitation tunnel and a towing tank, Renewable Energy 32 (2007) 407–426. doi:10.1016/j.renene.2006.01.012.

[3] A. Bahaj, L. Myers, Shaping array design of marine current energy converters through scaled experimental analysis, Energy 59 (2013) 83–94. doi:10.1016/j.energy.2013.07.023.

[4] F. Maganga, G. Germain, J. King, G. Pinon, E. Rivoalen, Experimental characterisation of flow effects on marine current turbine behaviour and on its wake properties, IET Renewable Power Generation 4 (2010) 498. doi:10.1049/iet-rpg.2009.0205.

[5] P. Mycek, B. Gaurier, G. Germain, G. Pinon, E. Rivoalen, Experimental study of the turbulence intensity effects on marine current turbines behaviour. part i: One single turbine, Renewable Energy 66 (2014) 729–746. doi:10.1016/j.renene.2013.12.036.

[6] B. Morandi, F. D. Felice, M. Costanzo, G. Romano, D. Dhomé, J. Allo, Experimental investigation of the near wake of a horizontal axis tidal current turbine, International Journal of Marine Energy 14 (2016) 229–247. doi:10.1016/j.ijome.2016.02.004.

[7] P. Mycek, B. Gaurier, G. Germain, G. Pinon, E. Rivoalen, Experimental study of the turbulence intensity effects on marine current turbines behaviour. part ii: Two interacting turbines, Renewable Energy 68 (2014) 876–892. doi:10.1016/j.renene.2013.12.048.

[8] M. Allmark, R. Ellis, T. Ebdon, C. Lloyd, S. Ordonez-Sanchez, R. Martinez, A. Mason-Jones, C. Johnstone, T. O'Doherty, A detailed study of tidal turbine power production and dynamic loading under grid generated turbulence and turbine wake operation, Renewable Energy (12 2020). doi:10.1016/j.renene.2020.12.052.

[9] T. Ebdon, M. Allmark, D. O'Doherty, A. Mason-Jones, T. O'Doherty, G. Germain, B. Gaurier, The impact of turbulence and turbine operating condition on the wakes of tidal turbines, Renewable Energy 165 (2021). doi:10.1016/j.renene.2020.11.065.

[10] Y. Chen, B. Lin, J. Lin, S. Wang, Experimental study of wake structure behind a horizontal axis tidal stream turbine, Applied Energy 196 (2017) 82–96. doi:10.1016/J.APENERGY.2017.03.126.

[11] I. Afgan, J. McNaughton, S. Rolfo, D. Apsley, T. Stallard, P. Stansby, Turbulent flow and loading on a tidal stream turbine by les and rans, International Journal of Heat and Fluid Flow 43 (2013) 96–108. doi:10.1016/j.ijheatfluidflow.2013.03.010.

[12] S. Tedds, I. Owen, R. Poole, Near-wake characteristics of a model horizontal axis tidal stream turbine, Renewable Energy 63 (2014) 222–235. doi:10.1016/j.renene.2013.09.011.

[13] T. Blackmore, W. M. Batten, A. S. Bahaj, Influence of turbulence on the wake of a marine current turbine simulator, Proceedings of the Royal Society A: Mathematical, Physical and Engineering Sciences 470 (10 2014). doi:10.1098/RSPA.2014.0331.

[14] Z. Zhang, Y. Zhang, J. Zhang, Y. Zheng, W. Zang, X. Lin, E. Fernandez-Rodriguez, Experimental study of the wake homogeneity evolution behind a horizontal axis tidal stream turbine, Applied Ocean Research 111 (6 2021).

[15] P. B. S. Lissaman, Energy effectiveness of arbitrary arrays of wind turbines, Journal of Energy 3 (1979) 323–328. doi:10.2514/3.62441.

[16] N. Jensen, A note on wind generator interaction, no. 2411 in Risø-M, Risø National Laboratory, 1983.

[17] S. P. O. R. S. L. J. H. M. T. Sten Frandsen, Rebecca Barthelmie, Analytical modelling of wind speed deficit in large offshore wind farms, Wind Energy 9 (2006) 39–53. doi:10.1002/we.189.

[18] M. Bastankhah, F. Porté-Agel, A new analytical model for wind-turbine wakes, Renewable Energy 70 (2014) 116–123. doi:10.1016/j.renene.2014.01.002.

[19] W.-H. Lam, L. Chen, Equations used to predict the velocity distribution within a wake from a horizontal-axis tidal-current turbine, Ocean Engineering 79 (2014) 35–42. doi:10.1016/j.oceaneng.2014.01.005.

[20] G. Pinon, P. Mycek, G. Germain, E. Rivoalen, Numerical simulation of the wake of marine current turbines with a particle method, Renewable Energy 46 (2012) 111–126. doi:10.1016/j.renene.2012.03.037.

[21] M. Allmark, R. Ellis, C. Lloyd, S. Ordonez-Sanchez, K. Johannesen, C. Byrne, C. Johnstone, T. O'Doherty, A. Mason-Jones, The development, design and characterisation of a scale model horizontal axis tidal turbine for dynamic load quantification, Renewable Energy 156 (2020). doi:10.1016/j.renene.2020.04.060.

[22] C. Lloyd, M. Allmark, S. Ordonez-Sanchez, R. Martinez, C. Johnstone, G. Germain, B. Gaurier, A. Mason-Jones, T. O'Doherty, Validation of the dynamic load characteristics on a tidal stream turbine when subjected to wave and current interaction, Ocean Engineering 222 (2021). doi:10.1016/j.oceaneng.2020.108360.

[23] S. Ordonez-Sanchez, M. Allmark, K. Porter, R. Ellis, C. Lloyd, I. Santic, T. O'Doherty, C. Johnstone, Analysis of a horizontal-axis tidal turbine performance in the presence of regular and irregular waves using two control strategies, Energies 12 (2019). doi:10.3390/en12030367.

[24] R. Martinez, S. Ordonez-Sanchez, M. Allmark, C. Lloyd, T. O'Doherty, G. Germain, B. Gaurier, C. Johnstone, Analysis of the effects of control strategies and wave climates on the loading and performance of a laboratory scale horizontal axis tidal turbine, Ocean Engineering 212 (2020) 107713. doi:10.1016/j.oceaneng.2020.107713.

[25] M. Allmark, R. Martinez, S. Ordonez-Sanchez, C. Lloyd, T. O'Doherty, G. Germain, B. Gaurier, C. Johnstone, A phenomenological study of

lab-scale tidal turbine loading under combined irregular wave and shear flow conditions, Journal of Marine Science and Engineering 9 (2021) 593. doi:10.3390/jmse9060593.

[26] R. Ellis, M. Allmark, T. O'Doherty, A. Mason-Jones, S. Ordonez-Sanchez, K. Johannesen, C. Johnstone, Design process for a scale horizontal axis tidal turbine blade, in: 4th Asian Wave and Tidal Energy Conference, TWN, 2018.
URL https://strathprints.strath.ac.uk/65920/

[27] T. Blackmore, L. E. Myers, A. S. Bahaj, Effects of turbulence on tidal turbines: Implications to performance, blade loads, and condition monitoring, International Journal of Marine Energy 14 (2016) 1–26. doi:10.1016/j.ijome.2016.04.017.

[28] A. Mason-Jones, D. O'Doherty, C. Morris, T. O'Doherty, C. Byrne, P. Prickett, R. Grosvenor, I. Owen, S. Tedds, R. Poole, Non-dimensional scaling of tidal stream turbines, Energy 44 (2012) 820–829. doi:10.1016/j.energy.2012.05.010.

[29] Y. Qian, Y. Zhang, Y. Sun, H. Zhang, Z. Zhang, C. Li, Experimental and numerical investigations on the performance and wake characteristics of a tidal turbine under yaw, Ocean Engineering 289 (2023) 116276. doi:10.1016/j.oceaneng.2023.116276.

[30] J. Schluntz, R. H. Willden, The effect of blockage on tidal turbine rotor design and performance, Renewable Energy 81 (2015) 432–441. doi:10.1016/J.RENENE.2015.02.050.

[31] J. I. WHELAN, J. M. R. GRAHAM, J. PEIRÓ, A free-surface and blockage correction for tidal turbines, Journal of Fluid Mechanics 624 (2009) 281–291. doi:10.1017/S0022112009005916.

[32] N. Kolekar, A. Vinod, A. Banerjee, On blockage effects for a tidal turbine in free surface proximity, Energies 12 (17) (2019). doi:10.3390/en12173325.
URL https://www.mdpi.com/1996-1073/12/17/3325

[33] H. Sarlak, T. Nishino, L. A. Martínez-Tossas, C. Meneveau, J. N. Sørensen, Assessment of blockage effects on the wake characteristics

and power of wind turbines, Renewable Energy 93 (2016) 340–352. doi:10.1016/J.RENENE.2016.01.101.

[34] P. Stansby, T. Stallard, Fast optimisation of tidal stream turbine positions for power generation in small arrays with low blockage based on superposition of self-similar far-wake velocity deficit profiles, Renewable Energy 92 (2016) 366–375. doi:10.1016/j.renene.2016.02.019.

[35] T. Burton, N. Jenkins, D. Sharpe, E. Bossanyi, Wind Energy Handbook, Wiley, 2011. doi:10.1002/9781119992714.

[36] M. S. Uberoi, P. Freymuth, Turbulent energy balance and spectra of the axisymmetric wake, The Physics of Fluids 13 (1970) 2205–2210. doi:10.1063/1.1693225.

[37] I. Wygnanski, F. Champagne, B. Marasli, On the large-scale structures in two-dimensional, small-deficit, turbulent wakes, Journal of Fluid Mechanics 168 (1986) 31. doi:10.1017/S0022112086000289.

[38] S. Cannon, F. Champagne, A. Glezer, Observations of large-scale structures in wakes behind axisymmetric bodies, Experiments in Fluids 14 (1993) 447–450. doi:10.1007/BF00190199.

[39] T. Stallard, T. Feng, P. Stansby, Experimental study of the mean wake of a tidal stream rotor in a shallow turbulent flow, Journal of Fluids and Structures 54 (2015) 235–246. doi:10.1016/j.jfluidstructs.2014.10.017.

[40] C. Jordan, D. Dundovic, A. K. Fragkou, G. Deskos, D. S. Coles, M. D. Piggott, A. Angeloudis, Combining shallow-water and analytical wake models for tidal array micro-siting, Journal of Ocean Engineering and Marine Energy 8 (2022) 193–215. doi:10.1007/s40722-022-00225-2.

[41] S. B. Pope, Turbulent Flows, Cambridge University Press, 2000. doi:10.1017/CBO9780511840531.

[42] H. Glauert, A general theory of the autogyro (1926).

[43] H. Schlichting, K. Gersten, Turbulent Boundary Layers Without Coupling of the Velocity Field to the Temperature Field, Springer Berlin Heidelberg, 2017, pp. 557–610. doi:10.1007/978-3-662-52919-5$_1$8.

[44] E. Jump, A. Macleod, T. Wills, Review of tidal turbine wake modelling methods, International Marine Energy Journal 3 (2020) 91–100. doi:10.36688/imej.3.91-100.

[45] O. D. Medina, F. G. Schmitt, R. Calif, G. Germain, B. Gaurier, Turbulence analysis and multiscale correlations between synchronized flow velocity and marine turbine power production, Renewable Energy 112 (2017) 314–327. doi:10.1016/j.renene.2017.05.024.

[46] A. Kolmogorov, Dissipation of energy in the locally isotropic turbulence, Proceedings of the Royal Society of London. Series A: Mathematical and Physical Sciences 434 (1991) 15–17. doi:10.1098/rspa.1991.0076.
URL `https://royalsocietypublishing.org/`

[47] K. S. Choi, J. L. Lumley, The return to isotropy of homogeneous turbulence, Journal of Fluid Mechanics 436 (2001) 59–84. doi:10.1017/S002211200100386X.
URL `https://www.cambridge.org/core/journals/journal-of-fluid-mechanics/article/re`

[48] Z. Zhang, Y. Zhang, J. Zhang, Y. Zheng, W. Zang, X. Lin, E. Fernandez-Rodriguez, Experimental study of the wake homogeneity evolution behind a horizontal axis tidal stream turbine, Applied Ocean Research 111 (2021) 102644. doi:10.1016/J.APOR.2021.102644.

[49] Y. Zhang, W. Zang, J. Zheng, L. Cappietti, J. Zhang, Y. Zheng, E. Fernandez-Rodriguez, The influence of waves propagating with the current on the wake of a tidal stream turbine, Applied Energy 290 (2021) 116729. doi:10.1016/J.APENERGY.2021.116729.

[50] P. K. Raushan, S. K. Singh, K. Debnath, Turbulent anisotropy and length scale variation over multiple shaped structure, Journal of Offshore Mechanics and Arctic Engineering 145 (12 2023). doi:10.1115/1.4057007/1159795.
URL `https://dx.doi.org/10.1115/1.4057007`

[51] E. Branlard, Theoretical Foundations for Flows Involving Vorticity, Springer, 2017, pp. 11–82. doi:10.1007/978-3-319-55164-7_2.